A NON-PYRAMIDAL RECTANGULAR-TO-TROUGH WAVEGUIDE TRANSITION AND PATTERN RECONFIGURABLE TROUGH WAVEGUIDE ANTENNA

A Thesis

by

LOIZOS LOIZOU

Submitted to the Office of Graduate Studies of
Texas A&M University
in partial fulfillment of the requirements for the degree of

MASTER OF SCIENCE

December 2010

Major Subject: Electrical Engineering

A Non-Pyramidal Rectangular-to-Trough Waveguide Transition and Pattern Reconfigurable Trough Waveguide Antenna

A NON-PYRAMIDAL RECTANGULAR-TO-TROUGH WAVEGUIDE TRANSITION AND PATTERN RECONFIGURABLE TROUGH WAVEGUIDE ANTENNA

A Thesis

by

LOIZOS LOIZOU

Submitted to the Office of Graduate Studies of
Texas A&M University
in partial fulfillment of the requirements for the degree of

MASTER OF SCIENCE

Approved by:

Co-Chairs of Committee,	Gregory H. Huff Robert D. Nevels
Committee Members,	Henry Pfister Othon Rediniotis
Head of Department,	Costas N. Georgiades

December 2010

Major Subject: Electrical Engineering

ABSTRACT

A Non-Pyramidal Rectangular-to-Trough Waveguide Transition and Pattern
Reconfigurable Trough Waveguide Antenna. (December 2010)

Loizos Loizou, Diploma, National Technical University of Athens

Co-Chairs of Advisory Committee: Dr. Gregory. Huff
Dr. Robert D. Nevels

Trough waveguides (TWG) have been utilized in a variety of radio frequency (RF) and other related applications including radar, the treatment of hypothermia and in the generation of plasmas. Perturbing the guided wave in these structures with blocks, rods, dielectrics, and other structures can create reconfigurable periodic line sources. These trough waveguide antennas (TWA) are then capable of providing both fixed-frequency and frequency-dependent beam steering. This was originally performed using electro-mechanical “cam-and-gear” mechanisms. Previous work related to the excitation of TWG and the performance of TWA topologies are limited when compared to more common antenna designs, yet they possess many desirable features that can be exploited in a modern system.

This thesis will examines an S-band rectangular-to-trough waveguide transition and trough guide antenna that has been designed for broadband reconfigurable antenna applications considering as well the airflow characteristics for sensing applications. The design, fabrication, and electromagnetic performance (mode conversion, impedance matching, and antenna performance) are discussed, including the use of metallic cantilever perturbations placed along the troughguide sidewalls that are designed to provide improved impedance matching when steering the beam from the backward quadrant through broadside, towards the forward quadrant. Impedance matching techniques such as use of circular holes at the edge of each actuated cantilever are used to reduce power reflections and provide a low voltage standing wave ratio (VSWR) along the S-band. Finite element simulations will provide a demonstration of the airflow and turbulence characteristics throughout the entire structure, where the metallic cantilevers are used to manipulate the flow of air, to distribute it across the surfaces of the structure better and improve its potential for sensing operations.

ACKNOWLEDGEMENTS

I would like to thank my committee co-chairs, Dr. Gregory Huff and Dr. Robert Nevels, and my committee members, Dr. Othon Rediniotis and Dr. Henry Pfister, for their guidance and support throughout the course of my research.

Thanks also go to my friends and colleagues and the department faculty and staff for making my time at Texas A&M University a great experience. Special thanks to S. A. Long, F. J. Drummond and S. A. Goldberger for their help and useful remarks during this procedure.

Finally, thanks to my mother and father for their encouragement and support.

NOMENCLATURE

TWA	Trough Wave Antenna
TWG	Trough Wave Guide
RWG	Rectangular Wave Guide
P	Pressure
T	Time
TEM	Transverse Electromagnetic
TE	Transverse Electric
TM	Transverse Magnetic
EM	Electromagnetics
VSWR	Voltage Standing Wave Ratio
RF	Radio Frequency
DUT	Device Under Test
UAV	Unmanned Aerial Vehicle
PIFA	Planar Inverted F-Antenna
GPS	Global Position System
WSN	Wireless Sensor Network
PDA	Personal Digital Assistant
BAN	Body Area Network
LWA	Leaky Wave Antenna

TABLE OF CONTENTS

Page

LIST OF FIGURES

Page

Page

Page

Page

CHAPTER I

INTRODUCTION

Cell phones, electronic personal assistants (PDAs), global position systems (GPS), wireless and satellite television represent just a few of the examples of the impact wireless communication systems have made on everyday life. Wireless sensor networks, a subset of wireless systems, have been developed to play an important role in personal and public safety. Applications range from body area networks (BAN) for remotely monitoring and treating a patient's health to more environmentally oriented applications such as temperature and humidity monitoring. Public safety applications include the detection of biological and chemical threats, toxins and poisons in air, and smoke for advanced fire safety and early warning measures. There are many other potential applications.

Modern technology is driven toward constant miniaturization and integration of systems and devices. Meeting the demands of the former may be limited by the size of larger system components such as antennas, whose efficiency and performance is predominantly dependent on their effective aperture size. Antenna designs such as microstrip patches and planar inverted F-antennas (PIFAs) have led to conformal planar topologies that help reduce their size, but there are still fundamental physical limits that exist and certain applications will almost always require larger antennas with higher gain and directivity. To this end, the structural and functional integration of several subsystems can result in technologies that can support the demands of these systems.

This thesis follows the style of IEEE Transactions on Antennas and Propagation.

Multifunctionality is a term describing this desire and the set of devices that can efficiently and simultaneously perform more than one function or operational objective; however, it can lead to a potentially complex integration process so the amalgamation of function must be done diligently. This work seeks to do this by blending antenna technologies amendable to the base stations of a wireless networks. These are commonly placed atop a rooftop, which provides an opportunity to include sensing mechanisms for measuring temperature, humidity in the air, and potentially the detection of smoke and/or poisonous gases. Future applications may also include the structural integration of these antennas into mobile platforms such as UAVS or even into high security buildings to detect weapons, explosives, chemical agents, biological threats, and possibly to perform imaging during sensing operations.

Trough waveguides (TWG) are open structures that offer 50% more bandwidth than regular waveguides (RWG). Any perturbation inside the TWG can cause radiation to leak out through the effective aperture (e.g., the open end of the structure) and create a trough waveguide antenna (TWA). This process of facilitating radiation in the TWA can be controlled, thereby making it possible to create a reconfigurable antenna from this design. This kind of large aperture antenna based on leaky-wave structures can also support multifunction operations in many microwave applications. It is well known that most leaky-wave antennas have a main beam which is scanned by applying a frequency sweep. Some of these structures can also been designed to provide beam steering for a fixed frequency; this reduces the use of phase shifters and large feed networks in some cases and minimizes the system losses. These losses are actually present in the other elements of the electromechanical system but they are removed from the flow or throughput of information that is the antennas primary function. By using an electromagnetically (EM) transparent cover (e.g., one that does not dramatically alter the performance of the antenna), the TWG structure can be sealed and pressurized fluids or gasses can be passed through it. More specifically, pressurized air can be guided through the TWA where sensors can be integrated inside the structure and passed to the antenna to transmit the information across a long distance.

This thesis discusses the electromagnetic and aerodynamic co-design of a non-pyramidal RWG-to-TWG transition and a fixed-frequency pattern reconfigurable TWA providing many of the desirable characteristics required by a platform which integrates reconfigurable antennas and sensing mechanisms into the same device. A review of the TWA and their applications is followed by the design, analysis, fabrication and evaluation procedures of an RWG-to-TWG transition examining both the electromagnetic and aerodynamic performance of the structure. The use of cantilever perturbations is then discussed for controlling the leaked power from the TWA for broadside radiation and pattern reconfigurable antennas (e.g., fixed frequency beam steering). An aerodynamic study of the structure investigates the airflow and turbulence characteristics throughout the entire RWG-to-TWG transition and within the TWA. The effect of the metallic cantilevers is also examined providing the means to control the flow of air, to better distribute it across the surfaces of the structure and improve its potential for sensing operations.

CHAPTER II

BACKGROUND

A. S-Parameters

Directly measuring the port currents and the voltages is not easily accomplished when dealing with high frequency networks so the scattering matrix, or *S*-matrix, is commonly used as a means of analysis. This measures the reflection and transmission at and between each port in the network, and provides a complete description of the network as seen at its *N*-ports. These *S*-parameters (the N^2 elements in an *N*-by-*N* *S*-matrix) are a measure of power that relate the incident and reflected voltage waves at each port with respect to their characteristic wave impedance. A diagram of an arbitrary *N*-port network is shown on Fig.1, where V_n^+ is the amplitude of the incident voltage wave on port *N* and V_n^- is the amplitude of the reflected wave from port *N*.

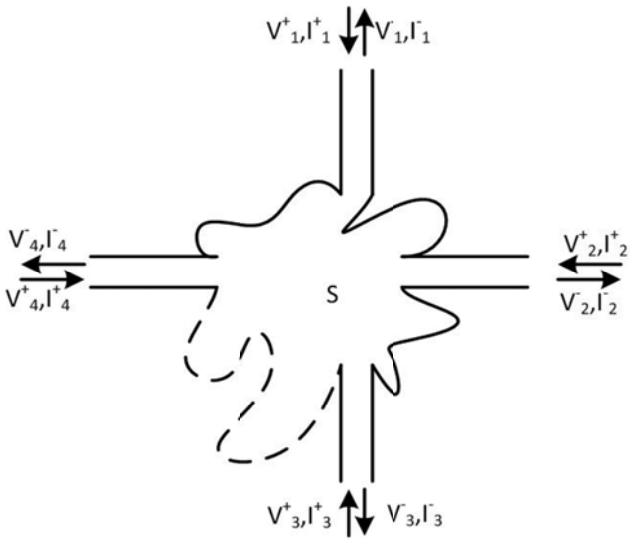

Fig. 1. An N port network showing the incident and reflected voltages and currents.

The S-matrix (1), or $[S]$, has elements given by (2). This illustrates that S_{ij} is found by applying a voltage V_j^+ to port *j* and getting a voltage V_i^- out of port *i*. The excitation on all the other ports is set to zero (also known as a matched termination condition) so S_{ij} gives the transmission coefficient from port *j* to port *i*. For reciprocal lossless networks, the elements in the S-matrix have the property shown in (3).

$$\begin{bmatrix} V_1^- \\ V_2^- \\ \vdots \\ V_n^- \end{bmatrix} = \begin{bmatrix} S_{11} & S_{12} & \cdots & S_{1N} \\ S_{21} & \ddots & & \vdots \\ \vdots & & \ddots & \vdots \\ S_{N1} & \cdots & \cdots & S_{NN} \end{bmatrix} \begin{bmatrix} V_1^+ \\ V_2^+ \\ \vdots \\ V_n^+ \end{bmatrix} \Rightarrow \left[V^-\right] = [S]\left[V^+\right] \tag{1}$$

$$S_{ij} = \frac{V_i}{V_j}\Big|_{V_k^+=0}, i \neq j \tag{2}$$

$$\begin{aligned} \sum_{k=1}^{N} S_{ki} S_{ki}^* &= 1, i = j \\ \sum_{k=1}^{N} S_{ki} S_{ki}^* &= 0, i \neq j \end{aligned} \tag{3}$$

Leaky-wave structures are typically *2*-port networks (e.g., $[S]$ is a 2x2 matrix) based on a transmission line topology, in which relatively large values of attenuation are due to radiation. The propagation characteristics in these leaky-wave structures are given by the complex propagation constant γ in (4), where α is the attenuation constant related to dissipated power (including radiation losses) and β is the phase constant that describes the propagation of EM energy within the structure. Each of these parameters is controllable through the design of the radiating or guiding structure.

$$\gamma = \alpha + j\beta \tag{4}$$

Fig. 2 illustrates the notional operation of a leaky-wave structure. Input and output power is measured at both ports of the structure allowing the calculation of the reflected and transmitted power often given in the form of return loss and insertion loss. The reflection coefficient for such structure is defined as the ratio of the reflected wave over the incident wave with port-*2* terminated with a matched load. The transmission coefficient is the ratio of the transmitted (measured from port-2) wave over the incident.

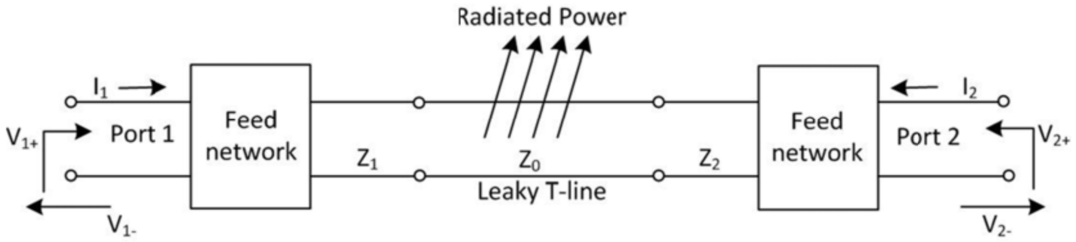

Fig. 2. A 2-port network representation of a leaky wave structure.

The reflection coefficient S_{11} characterizes the impedance match of an antenna and gives a measure of the delivered power. An impedance match results in $\Gamma=0$ and total reflection results in $\Gamma=1$. For circuit quantities this is given by (5).

$$\Gamma = \frac{Z_L - Z_o}{Z_L + Z_o} \tag{5}$$

The SWR (Standing Wave Ratio) is the amplitude of a partial standing wave at a maximum to the amplitude at a minimum, in a transmission line. It is often referred to as Voltage Standing Wave Ratio (VSWR). The SWR is related to Γ by (6). From a practical standpoint, it is desirable to minimize the standing waves on a device.

$$SWR = \frac{|\Gamma| + 1}{|\Gamma| - 1} \tag{6}$$

B. The ABCD Matrix

The *ABCD* matrix is convenient to use for cascade *2*-port networks. For a *2*-port network the *ABCD* matrix is defined as follows (7) according to Fig. 3, where the matrix form is given by (8).

$$\begin{aligned} V_1 &= AV_2 + BI_2 \\ I_1 &= CV_2 + DI_2 \end{aligned} \tag{7}$$

$$\begin{bmatrix} V_1 \\ I_1 \end{bmatrix} = \begin{bmatrix} A & B \\ C & D \end{bmatrix} \begin{bmatrix} V_2 \\ I_2 \end{bmatrix} \tag{8}$$

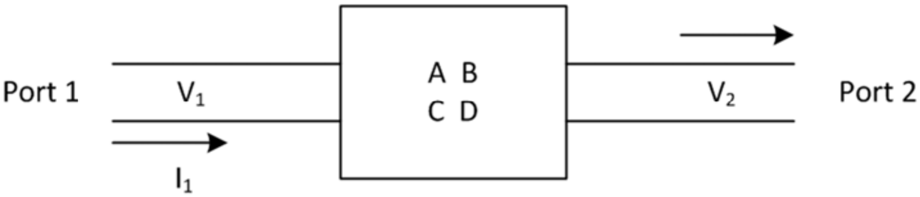

Fig. 3. An ABCD matrix representation of a 2-port network.

Fig.4 illustrates a *2*-port network and how the *2*-port parameters of the device under test (DUT) may be obtained by applying inverse matrices to the measurement to effectively remove unwanted, external hardware from the measurement. This is especially useful for de-embedding theses unwanted effects from a measurement.

$$\begin{gathered} \begin{bmatrix} V_1 \\ I_1 \end{bmatrix} = \begin{bmatrix} A_1 & B_1 \\ C_1 & D_1 \end{bmatrix} \begin{bmatrix} V_2 \\ I_2 \end{bmatrix} \\ \begin{bmatrix} V_2 \\ I_2 \end{bmatrix} = \begin{bmatrix} A_2 & B_2 \\ C_2 & D_2 \end{bmatrix} \begin{bmatrix} V_3 \\ I_3 \end{bmatrix} \\ \begin{bmatrix} V_1 \\ I_1 \end{bmatrix} = \begin{bmatrix} A_1 & B_1 \\ C_1 & D_1 \end{bmatrix} \begin{bmatrix} A_2 & B_2 \\ C_2 & D_2 \end{bmatrix} \begin{bmatrix} V_3 \\ I_3 \end{bmatrix} \end{gathered} \tag{9}$$

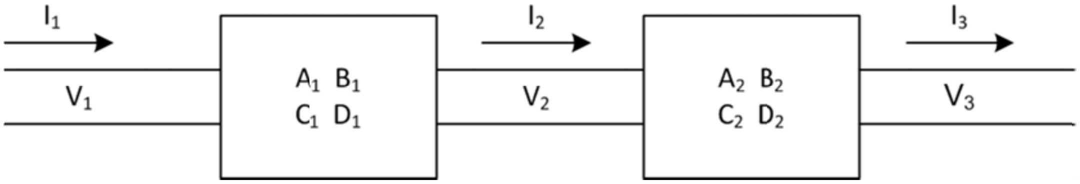

Fig. 4. Casketed 2-port networks.

As an example consider the *2*-port network of Fig. 5, which represents a DUT connected at both ends to transitions which are connected to the feed networks and transitions. This setup resembles the experimental setup being used in this work. The *S*-parameters of the transitions can be easily measured individually, by connecting them back-to-back. Having that measurement, the *S*-parameters of the overall system of Fig. 5 can then be measured. Using the appropriate methodology the *S*-parameters can be transferred to *ABCD* and using (10) can be used to specify the *ABCD* matrix of the DUT which again can be transferred back to *S*-parameters.

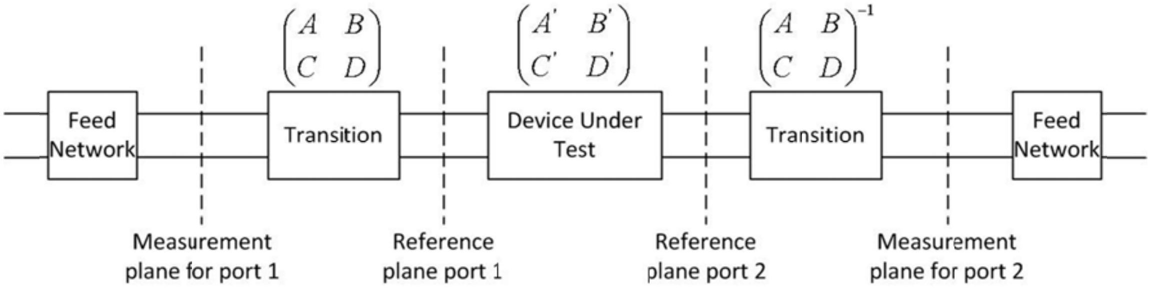

Fig. 5. A deembeded 2-port cascaded network.

$$\begin{pmatrix} A^m & B^m \\ C^m & D^m \end{pmatrix} = \begin{pmatrix} A & B \\ C & D \end{pmatrix} \begin{pmatrix} A' & B' \\ C' & D' \end{pmatrix} \begin{pmatrix} A & B \\ C & D \end{pmatrix}^{-1} \tag{10}$$

C. Waveguides

The foundation of all leaky wave antennas is a transmission line or modal wave-guiding structure. One of the most basic waveguides and the platform for much of the designs in the literature is the RWG shown in Fig. 6. Many antenna designs take this simple structure and add perturbations such as slots along the longitudinal and/or broad walls (described later). The structure supports modal field distributions that are either TE (transverse electric, with $E_z = 0$) or TM (transverse magnetic, with $H_z = 0$) modes. The fields components for the TE_{mn} mode are given by (11), with m and n being the mode indices, A_{mn} the modal weighting coefficient, and β (for the lossless case $\alpha = 0$) by (12).

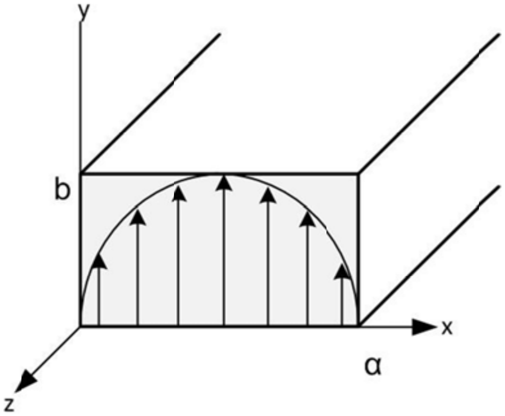

Fig. 6. A rectangular waveguide showing the fundamental mode.

$$
\begin{aligned}
H_Z &= A_{mn}\cos\frac{m\pi x}{a}\sin\frac{n\pi y}{b}e^{-j\beta z} \\
E_x &= \frac{j\omega\mu n\pi}{k_c^2 b}A_{mn}\cos\frac{m\pi x}{a}\sin\frac{n\pi y}{b}e^{-j\beta z} \\
E_y &= \frac{-j\omega\mu m\pi}{k_c^2 a}A_{mn}\sin\frac{m\pi x}{a}\cos\frac{n\pi y}{b}e^{-j\beta z} \\
H_x &= \frac{j\beta m\pi}{k_c^2 a}A_{mn}\,\mathrm{c}\sin\frac{m\pi x}{a}\cos\frac{n\pi y}{b}e^{-j\beta z} \\
H_y &= \frac{j\beta n\pi}{k_c^2 b}A_{mn}\cos\frac{m\pi x}{a}\sin\frac{n\pi y}{b}e^{-j\beta z}
\end{aligned}
\tag{11}
$$

$$
\beta = \sqrt{k^2 - k_c^2} = \sqrt{k^2 - (\frac{m\pi}{a})^2 - (\frac{n\pi}{b})^2} \tag{12}
$$

The attenuation constant α accounts for ohmic and radiation losses, so for most materials (i.e. copper and aluminum) the ohmic losses are very small compared to radiation from the guide. Hence, this work seeks to maximize the equivalent α. The wave impedance of a waveguide is also an important quantity, and is given by (13), where $\omega = 2\pi f$ with f as the operational frequency, μ the permittivity and n the impedance of free space. The characteristic impedance of the waveguide Z_0 is given by (14), where B is a constant depended on the b dimension of the guide [1]. Each mode in the waveguide has a cutoff frequency $f_{c,mn}$ (15). Frequencies below $f_{c,mn}$ cannot propagate in the corresponding mn mode. Frequencies below the lowest f_c (typically the TE_{10} illustrated in Fig. 6) are in cut-off and will not propagate. Typically, the waveguide's dimensions are selected to allow operation within the band of interest ($f_{c,10} < f_{band} <$ higher order f_c). The separation between the lowest, or fundamental mode, and second lowest mode's f_c provide the concept of bandwidth for the waveguide.

$$Z_w(TE_{mn}) = \frac{E_x}{E_y} = \frac{\omega\mu}{\beta_Z} = \frac{n}{\sqrt{1-\left(\frac{f_c}{f}\right)^2}}, f > f_c \tag{13}$$

$$Z_0 = BZ_w \tag{14}$$

$$f_{c_{mn}} = \frac{k_c}{2\pi\sqrt{\mu\varepsilon}} = \frac{1}{2\pi\sqrt{\mu\varepsilon}}\sqrt{(\frac{m\pi}{a})^2 + (\frac{n\pi}{b})^2} \tag{15}$$

D. Leaky-Wave Antennas (LWA)

Leaky wave structures are characterized by a complex propagation wave number (4). The attenuation constant α is related to the radiation efficiency of the antenna and combined with the effective aperture to the beamwidth. The phase constant β, depends on frequency and is related to the direction of the beam, so leaky wave antennas can be scanned with frequency.

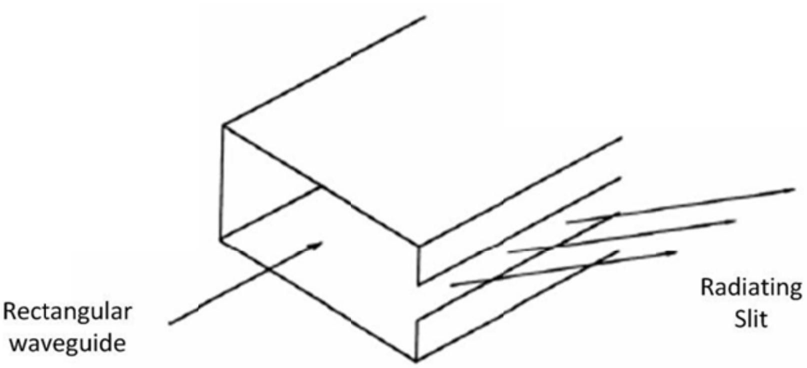

Fig. 7. A RWG with a radiating slit on the side (from [2]).

Tapering the effective aperture of the structure gives control over the side lobe level often creating a narrow pencil beam on the scan plane. The cross plane radiation is a fan shape beam. Techniques exist in the literature for narrowing the cross plane beam, and even permit 2-dimensional scanning. Many leaky wave structures differ from their early designs based on waveguides with long slits. Such devises are the trough waveguide antenna, the groove guide, the microstrip line and others.

Two types of leaky wave antennas exist and differ in both geometry and operation: periodic and uniform. Each provides some differences in performance. The uniform type has a uniform geometry along its length and can scan in the first quadrant from endfire close to broadside region, with a constant beamwidth. The periodic type has a periodic geometry, which is responsible for radiation and can scan almost all the backward and some of the forward quadrant.

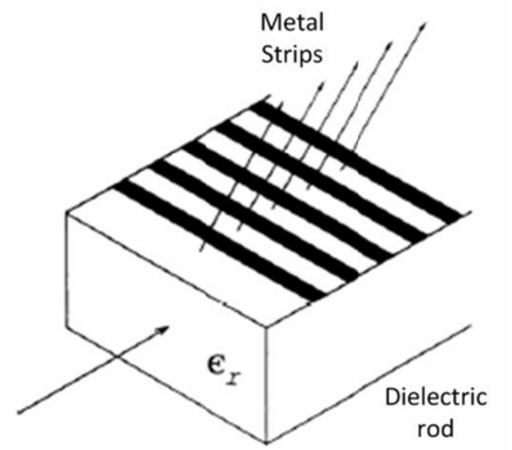

Fig. 8. A rectangular dielectric rod with an array of metal strips (from [2]).

E. Uniform Leaky-Wave Antennas

For an antenna of effective aperture length L, and depending on the application, α and β are determined theoretically or experimentally to functionally describe the design.

The main beam's direction is then given by (16) with a beamwidth from (17) using the free-space wave number (18). The maximum angle of the beam from broadside direction is ϑ_m, with (19) a condition to ensure 90% of the input power is radiated.

$$\sin \vartheta_m = \frac{\beta}{k_o} \tag{16}$$

$$\Delta\vartheta \sim \frac{1}{\left(\frac{L}{\lambda_o}\right)\cos \vartheta_m} \tag{17}$$

$$k_o = \frac{2\pi}{\lambda_o} \tag{18}$$

$$\frac{L}{\lambda_o} = \frac{0.18}{\frac{\alpha}{k_o}} \tag{19}$$

Scan angle ϑ_m behavior depends on the topology of the uniform leaky wave antenna. For an air filled guide the variation of scan angle with frequency is slower compared with the partially dielectric- filled type of waveguide. The radiation pattern is found by the Fourier transform of the aperture distribution and for an infinite antenna length (20); tapering the amplitude of this distribution can reduce the sidelobe level.

$$R(\vartheta) \sim \frac{\cos^2 \vartheta}{\left(\frac{\alpha}{k_o}\right)^2 + \left(\frac{\beta}{k_o} - \sin \vartheta\right)^2} \tag{20}$$

F. Periodic Leaky-Wave Antennas

In contrast to the uniform LWA, the periodic LWA topologies are modulated in a repetitive distribution along their length. The leakage mechanism is also different in a sense that uniform antennas support a “fast” mode which radiates. On the other hand, the dominate mode in a periodic structure needs to be introduced since it is a “slow” structure. The introduction of a periodic array in the guide perturbs the bounded mode in a manner that introduces an infinite number of space harmonics which are related to each other by (21), where $d = \frac{1}{f_o}$ is the period and β_o is the fundamental space harmonic.

$$\beta_n d = \beta_o d + 2\pi n \tag{21}$$

If one of the space harmonics becomes fast, radiation is achieved. Since only one beam is desirable, the integer *n* = -1 is chosen and for a frequency sweep this beam will emerge from backfire and sweep through broadside towards the forward quadrant. The resulting beam direction is determined by (22) with $\beta_{-1} = \beta_o - \frac{2\pi}{d}$ and $d = \frac{1}{f_o}$.

$$\sin \vartheta_m = \frac{\beta_{-1}}{k_o} = \frac{\lambda_o}{\lambda_g} - \frac{\lambda_o}{d} \tag{22}$$

G. Phase Accumulation

The radiation mechanism previously described explains the "open stop band" region which occurs in such periodic structures at a narrow region around broadside where resonant lengths are required for broadside radiation. The system can be seen as a cascaded circuit of transmission lines connected to similar loads and shown in Fig. 9. At broadside where the elements of the periodic array are exactly half a wavelength (*λ/2*) long each transmission line is then *λ/2* long. The total transmission of the system is then given by (23). This means that the total reflection seen at the input of the system is the sum of the reflections from reactive loads *Y.* Each of these shunt loads contributes to a total reflection coefficient (24). Most of the power delivered to the structure will be reflected (giving a high VSWR) when the beam scans through broadside.

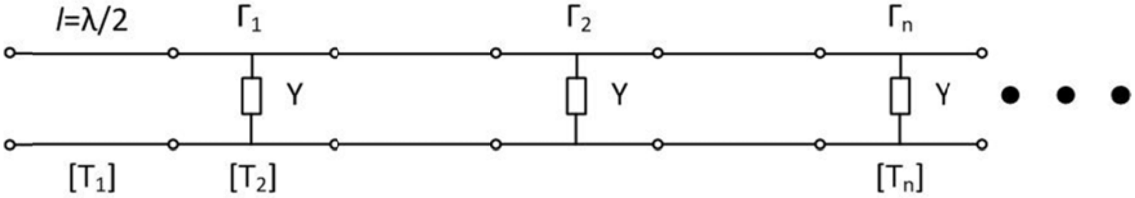

Fig. 9. Reflection from cascaded transmission line sections.

$$\begin{aligned}[T_{tot}] = [T_1][T_2]\ldots[T_n] &= \begin{pmatrix} \cos\beta l & jZ_o \sin\beta l \\ jY_o \sin\beta l & \cos\beta l \end{pmatrix} \begin{pmatrix} 1 & 0 \\ Y & 1 \end{pmatrix} \ldots \\ &= \begin{pmatrix} \cos\frac{2\pi}{\lambda}\frac{\lambda}{2} & jZ_o \sin\frac{2\pi}{\lambda}\frac{\lambda}{2} \\ jY_o \sin\frac{2\pi}{\lambda}\frac{\lambda}{2} & \cos\frac{2\pi}{\lambda}\frac{\lambda}{2} \end{pmatrix} \begin{pmatrix} 1 & 0 \\ Y & 1 \end{pmatrix} \ldots \\ &= \begin{pmatrix} 1 & 0 \\ 0 & 1 \end{pmatrix} \begin{pmatrix} 1 & 0 \\ Y & 1 \end{pmatrix} \begin{pmatrix} 1 & 0 \\ 0 & 1 \end{pmatrix} \begin{pmatrix} 1 & 0 \\ Y & 1 \end{pmatrix} \ldots = \begin{pmatrix} 1 & 0 \\ Y & 1 \end{pmatrix}^n \end{aligned} \tag{23}$$

$$\Gamma_{tot} = \sum_{0}^{\mathrm{N}} \Gamma_{\mathrm{N}} \tag{24}$$

H. Trough Waveguide Antennas (TWA)

Trough waveguides have been around for some time and have been extensively studied in the past as antennas, filters and other microwave applications. Rotman and Oliner [3] were able to alter the propagation characteristics of the guide by modifying the center fin. An array of circular holes and an array of teeth are the basic geometries studies for antenna scanning and filtering applications as seen at Fig.10.

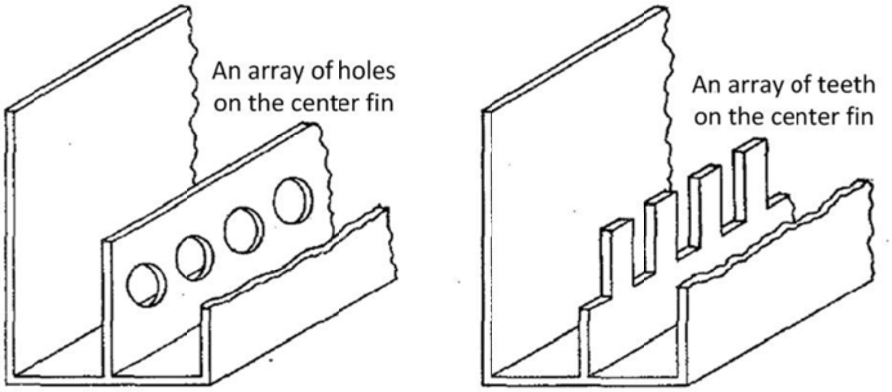

Fig. 10. TWA with arrays of holes and teeth (from [3]).

TWG are open structures but they do not radiate efficiently without the use of these perturbations. Rotman and Karas [4] introduced some microwave antenna designs and came to a series of useful conclusions regarding their functionality; namely that antisymmetric obstacles in TWA couple energy between the bound TE mode and the unbound TEM mode, and symmetric obstacles can be used for tuning. The horizontal rod combined with a vertical rod in Fig. 11 (middle) facilitates a resonant radiating element. A series of perpendicularly placed teeth on the center fin, Fig. 11 (left) causes radiation as well as a continuous asymmetry on one side of the TWA. A series of vertical teeth (Fig. 11, right) make the TWA a slow wave structure.

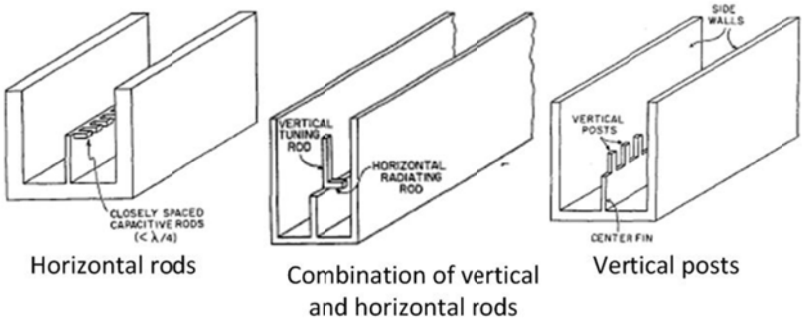

Fig. 11. TWA with vertical and horizontal rods on the center fin (from [4]).

Rotman and Maestri reported a “scannable” array in [5]; this was achieved by changing the phase velocity in the guide. The first method used to achieve this behavior was based on the rotation of symmetrical structures along the axis of the guide. The second was to vary the height of an array of teeth placed on the top of the center fin. If the TW is made continuously asymmetric the direction of the main beam for a fixed frequency is given by (25) where ϑ is the beam angle (limited to the near end fire region), λ_o is the free space wavelength, and λ_g is the guided wavelength.

$$\sin\vartheta = \frac{\lambda_o}{\lambda g} \tag{25}$$

If the TW is made partially asymmetric near broadside radiation is achieved and the angle of the main beam for a fixed frequency is given by (26), where l is the length of the perturbation. In this prior work the beam is scanned by applying a frequency sweep on a fixed setup and using metallic blocks as perturbations with a variable height that changes the guided wavelength. By changing the frequency or height the electrical length of the blocks changes, effectively scanning the beam away from broadside where the length of each block is seen to be half free-space wavelength.

$$\sin\vartheta = \frac{\lambda_o}{\lambda g} - \frac{\lambda_o}{2l} \tag{26}$$

In a more extensive work, Rotman and Oliner [6] present two types of leaky wave antennas based on the TWA. One made continuously asymmetric for end-fire radiation and another made periodically asymmetric for broadside radiation. An equivalent transmission line circuit is presented as seen in Fig. 12 along with an analytical model using the transverse resonance technique.

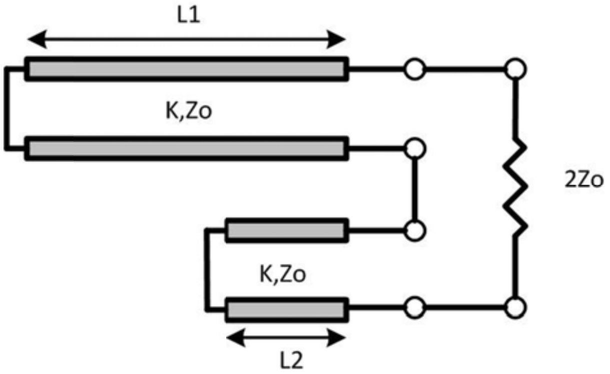

Fig. 12. An equivalent transmission line circuit of the TWG.

Furthermore to address the high reflections due to phase accumulation which occurs at broadside the use of tuning posts, Fig. 13(right) on the center fin was proposed. In a later work Huff and Long [7] studied the effect of the aperture distribution for reconfigurable radiation using cantilever perturbations for fixed frequency beam steering of a W-band trough waveguide antenna. It was shown that tapering the shape of the cantilevers improves the radiation behavior away from broadside but increases the side lobe level at broadside. This work also examined the use of variable-length perturbation to scan the beam.

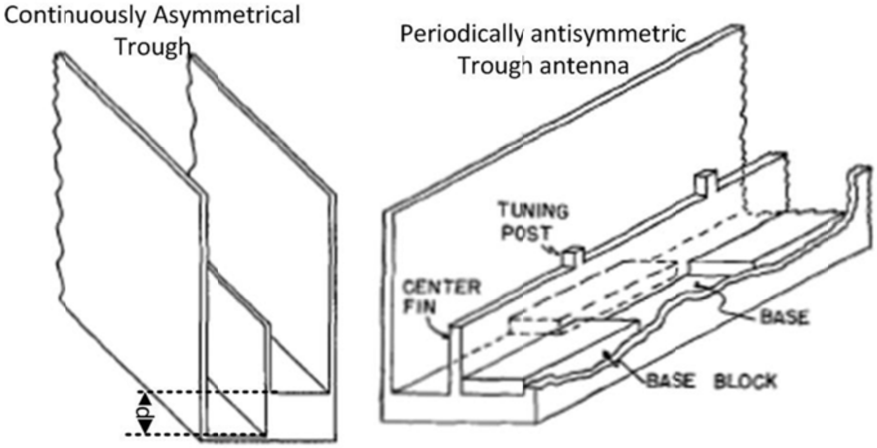

Fig. 13. A continuously asymmetric trough and a periodically antisymmetric trough (from [5]).

I. Antenna Measurements

The method used in this work to measure the radiation pattern of the prototype antenna is the Gain-Transfer method. A standard gain antenna is used to determine absolute gains. During this procedure two sets of measurements are made. For the first set the DUT (e.g., the TWA) is a receiving antenna that is placed on a rotating fixture at a distance R from a standard gain antenna where the received power is measured (P_t). For the second measurement the DUT is replaced by another standard gain antenna and the received power (P_S) is again measured. Since the standard gain (G_S) antenna is of known gain (G_T) the gain of the DUT can be calculated using by (27).

$$G_T(dB) = G_s(dB) + P_T(dB) - P_S(dB) \tag{27}$$

J. Aerodynamic Concepts

The aerodynamic behavior of this structure is also of interest to this work. The viscosity is an important parameter since it characterizes the internal resistance to flow within the structure. It also plays a significant role along with the velocity of the airflow and geometry confining the flow, which is described by two regimes – laminar and turbulent. Laminar flow occurs when a fluid flows in parallel layers or sheets, with no significant disruption between the layers. It is characterized by high momentum diffusion and low momentum convention. Flow is this regime usually corresponds to low Reynolds numbers (28); a dimensionless number that gives a measure of the ratio of inertial forces $\rho V^2 L^2$ to viscous forces μVL and quantifies the relative importance of these two types of forces for given flow conditions. It is used to characterize flow regime by linking the fluid density ρ, viscosity μ, velocity V, characteristic dimension L. For rectangular pipes and structures, the characteristic dimension is given by the hydraulic diameter D_H (29) with A as the cross sectional area and P as the wetted perimeter. Turbulent is then oppositely characterized by chaotic, stochastic property changes and dominated by inertial forces which result to random eddies, vortices and other flow instabilities. Turbulent flow is characterized by a high Reynolds number.

$$\mathrm{Re} = \frac{\rho VL}{\mu} \tag{28}$$

$$D_H = \frac{4A}{P} \tag{29}$$

CHAPTER III

A NON-PYRAMIDAL RECTANGULAR-TO-TROUGH WAVEGUIDE TRANSITION

A. Introduction

The TWAs in [3]-[4] have been utilized in a variety of antenna and other related applications including radar, the treatment of hypothermia [8], and in the generation of plasmas [9]. Excitation of the TWG from transmission line topologies like coaxial in [4] and [10], and guiding structures like RWG [8] are common. The latter requires a transition for broadband mode conversion and/or impedance transformation, which in-turn presents a key challenge towards their effectiveness in many of these previous applications.

A candidate rectangular-to-trough waveguide transition was designed to provide the excitation to a TWG and a TWA with reconfigurable radiation characteristics. It was also desired that air can flow through the TWA to be turbulent around perturbation for their dual purpose in sensing operations. The proposed transition provides impedance transformation and mode conversion across the full waveguide band (S-Band) for the TWG antenna structure under consideration. This section first presents the transition and discusses its operation as a mode converter and impedance transformer; a small degree of physical insight into the design of the transition design is presented in an attempt to provide a more comprehensive and useful discussion. The measured and simulated results for an S-band design are presented next. A study of the aerodynamic performance of the structure follows and results are shown and compared for two deferent lengths of this transition under different conditions.

B. Transition Topology and Operation

Fig. 14 shows the CAD model of the proposed RWG-to-TWG transition. It has a length L and a metal thickness t that remains uniform throughout the structure. The outer perimeter of the transition provides a linear taper between the RWG dimensions a_1 and b_1 and the TWG dimensions $2b_2 + t$ and a_2. Flaring between the widths a_1 and $2b_2$ (the top and bottom walls) remains symmetric about the center fin throughout the transition. However, flaring between the heights b_1 and a_2 (the side walls) is upward-directed to maintain a flat mounting surface at the bottom of the structure (with respect to open end, or top surface, of the TWG). The septum tapers linearly from a height of zero at the RWG port to the fin height s at the TWG port. It also occurs in an upward direction from the bottom of the structure.

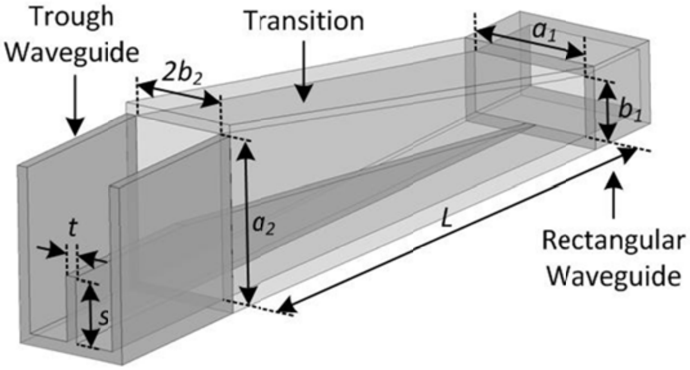

Fig. 14. CAD model of the non-pyramidal rectangular-to-trough waveguide transition.

Fig. 15 shows a conceptual view of the electric field distribution within the trough waveguide (left), transition (middle), and rectangular waveguide (right). If the dimensions of the TWG and RWG are fixed, the dimension *L* and its taper profile represent the only degrees of freedom in the design of the broadband transition. As such, both the impedances and field (mode) configurations must be transitioned through it.

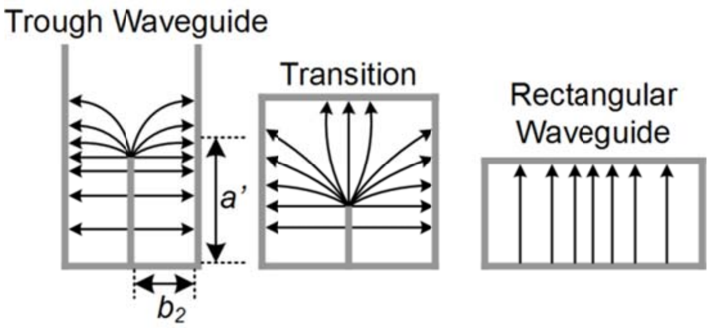

Fig. 15. Distribution of the electric field within the trough waveguide (left), transition (middle) and rectangular waveguide (right).

Observations [11] and prior work on linear and stepped tapered septums provide sufficient evidence that the tapered fin in Fig. 1 acts as a dual-polarizer rotator [12]-[15] (RWG-to-TWG mode conversion). The transition's cross-section resembles a flaring single ridge waveguide [16]-[17]. The narrow fin width *t* creates deviation from the confidence in this model but trends remain similar.

This corroborates with the more conceptual view of the transition using port-impedances. On the TWG side, the fin height can be extended to *a'* and a magnetic wall can be placed across the guide to approximate each trough as a closed structure [5]. These can each be treated analytically as two waveguides that support quarter-wave modes, with a TE_{10} cut-off condition approximated by $\lambda_{c10} \sim 4a'$. In addition to accurately predicting the TWG cut-off conditions this provides that each of the troughs can be considered in parallel, Fig. 16 (left), from an impedance point of view forming a rectangular waveguide as seen in Fig. 16(right) with $b=b_2$ and $a'=2(s+\delta+t)$. The variable δ represents a shift of the reference plane due to fringing effects [5]. This arrangement and their connection through a plane of electrical symmetry at the center of the TWG indicate that their combined impedance can be approximate by the impedance of a rectangular waveguide.

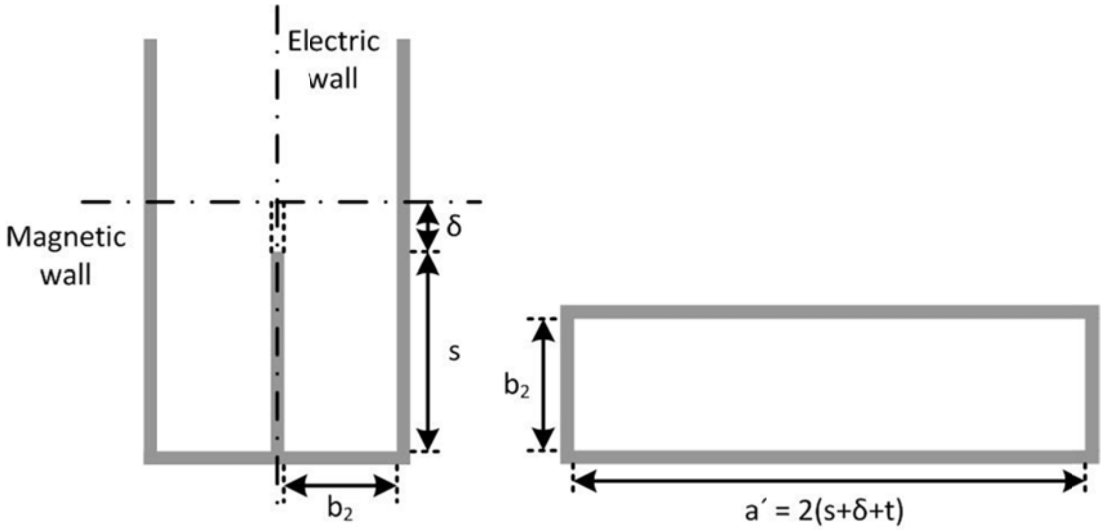

Fig. 16. The trough waveguide (left) as an equivalent rectangular waveguide (right).

Fig. 17 represents the real component of the impedance for the transition with respect to its length at 3GHz. At the TWG side (L = 0 mm) the impedance is approximated as the rectangular waveguide of Fig. 16 (right). Moving towards the center the simulated and calculated results deviate until the model breaks down in the middle of the structure where mode conversion and rotation occurs. Starting from RWG side (*L*= 320 mm) calculations neglect the presence of the center fin; this follows the simulated results for a small distance into the guide before the structure of the fields is changed due to the growing height of the septum.

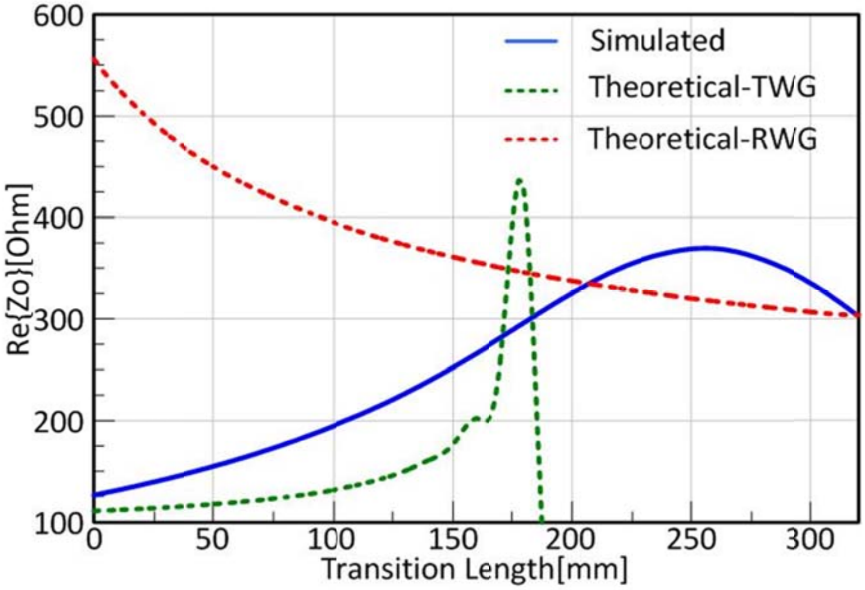

Fig. 17. Real part of the impedance with respect to transition's length.

C. Fabricated Transition and Results

The choice of the length (*L*) was based on simulations [11]-[18] of the electromagnetic and aerodynamic performance from which the shortest possible length providing large Bandwidth and low average VSWR, (Fig. 18), and at the same time provide turbulence and air circulation was selected to be 32 cm. This transition length provides an average VSWR less than 1.1 across the S-Band and a 2:1 VSWR Bandwidth of 2.33 GHz. Fig. 19 shows end-on views of the resulting CAD model for the S-band transition with the custom TWG antenna flange (top-left) and circular WR-284 flange (top-right), and the back-to-back arrangement of fabricated transitions used for measurements is shown in Fig. 20. The transition's parameters are: (a_1, b_1) = (7.214 cm, 3.404 cm), (a_2, $2b_2$) = (9.3 cm, 4.8 cm), and L = 32 cm.

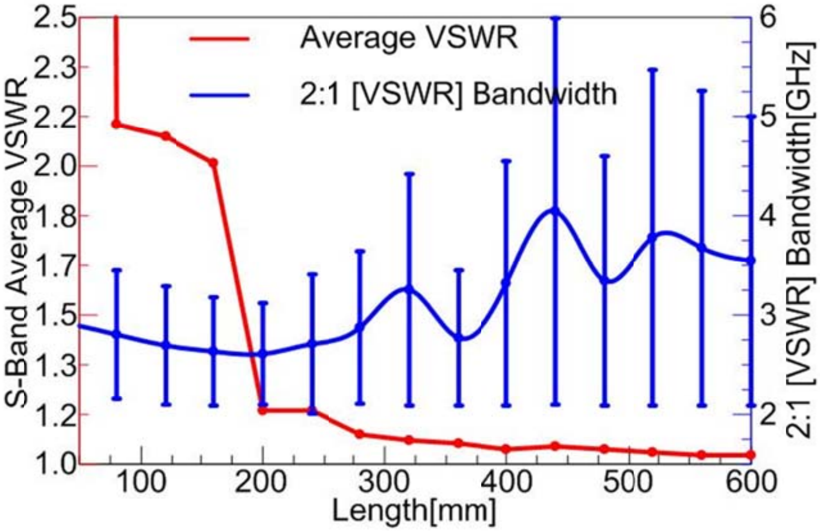

Fig. 18. Average VSWR and 2:1 VSWR bandwidth with respect to the transition length.

Each wall was mechanically milled from an aluminum plate with t = 6.35 mm, and mechanically assembled by periodically drilling and tapping 3.45 mm diameter holes for machine screws. Fig. 21 shows a cut of the three dimensional transition drawing where the center fin along the length is seen with screw holes coming from the bottom up to connect it to the bottom plate. The custom flange attached on the outer side of the structure is seen with an array of screws and 1/4 in. holes to connect to the TWA.

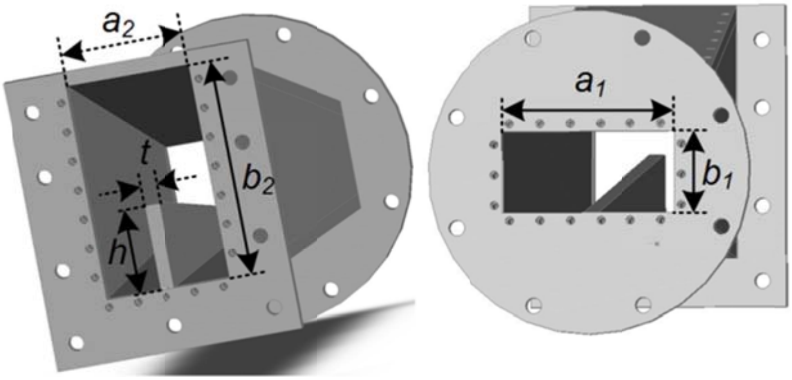

Fig. 19. The end-on views of the transition.

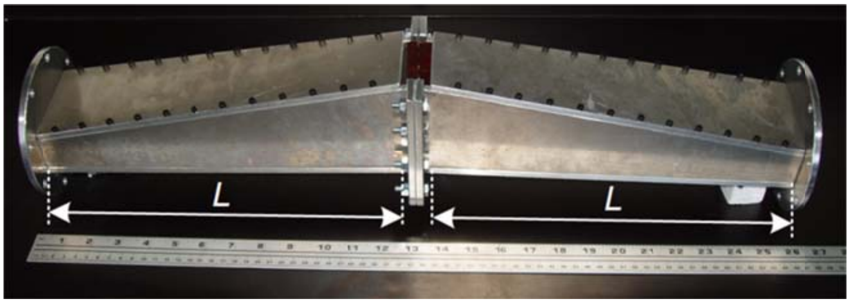

Fig. 20. Two fabricated S-band transitions in back-to-back arrangement.

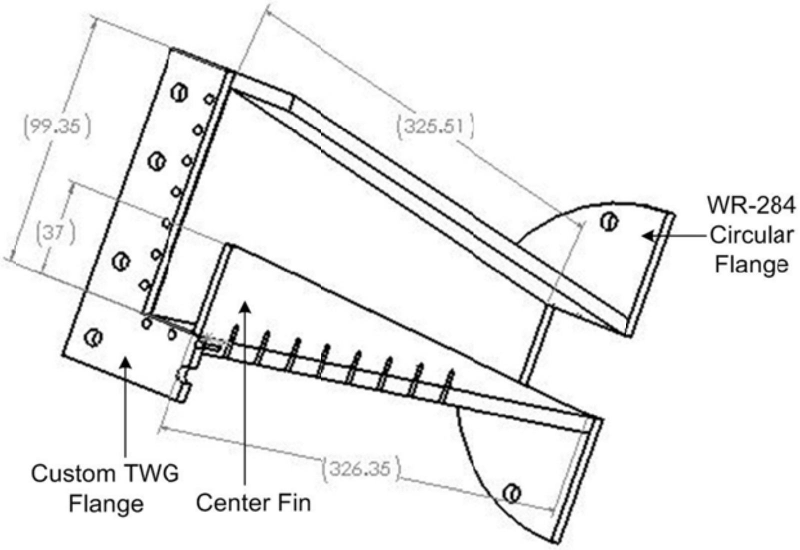

Fig. 21. A cut of the three dimensional drawing of the transition.

The simulated and measured results shown in Fig. 22 are for the back-to-back structure. Measurements were taken on an Agilent Technologies E8361C network analyzer which was calibrated using an S-Band waveguide calibration kit. These are in good agreement with simulated results and show less than 0.5 dB of insertion loss across the desired S-Band (2.6 GHz to 3.95 GHz). Major deviations are attributed to fabrication tolerances and the connection of the fin to the ground where screws were not possible due to the shallow height of the fin. Fig. 23 shows the simulated and measured results of a single transition. The deembedding procedure included the transformation of the measured *S*-parameters to *ABCD*-parameters in order to split into half the cascaded network. A Matlab script used for this purpose is included in Appendix A. Simulated and measured results are also in close agreement for this.

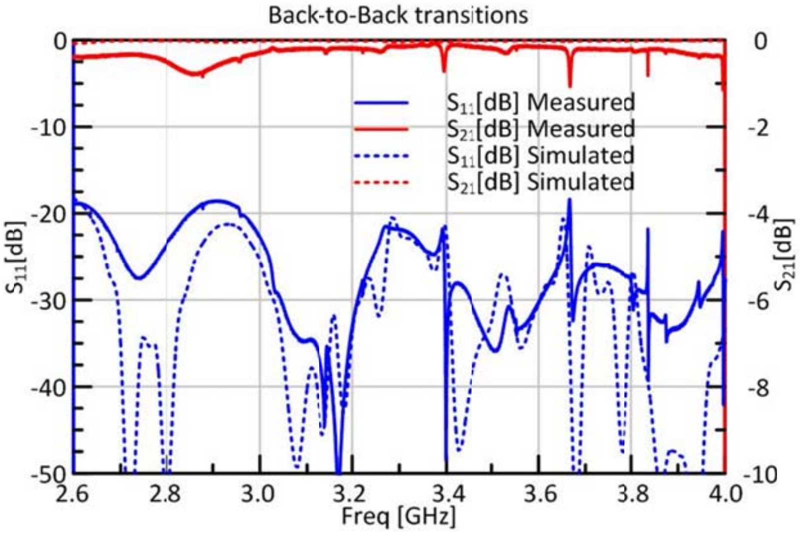

Fig. 22. Measured and simulated results for the back-to-back transition.

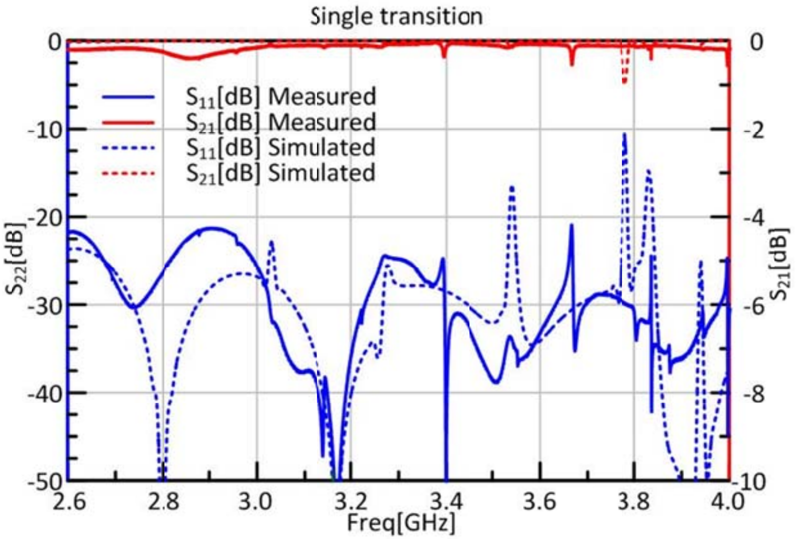

Fig. 23. Measured and simulated results for a single transition.

D. Aerodynamic Performance

The aerodynamic performance of the structure was examined [18] for several different inlet velocities: a light breeze ($V = 0.1$ m/s), a strong breeze at ($V = 1$ m/s), a car in an urban area at ($V = 10$ m/s), a car on a freeway driving at ($V = 25$ m/s), an unmanned aerial vehicle (UAV) ($V = 45$ m/s), and a category 4 hurricane ($V = 61$ m/s). The magnitude of the velocity, vorticity and turbulent kinetic energy are shown for both the inlet and the outlet of the transition for these scenarios in Figs. 24-29, respectively, for air with $\rho = 1.19$ kg/m^3 and $\mu = 1.8\text{e-}5$ Pa·s. These plots also show the fabricated design with $L = 320$ mm (left) and a shorter transition with $L = 160$ mm and equivalent EM performance (right). The comparison in length is meant to illustrate the need to co-design for different modalities in a multifunctional structure.

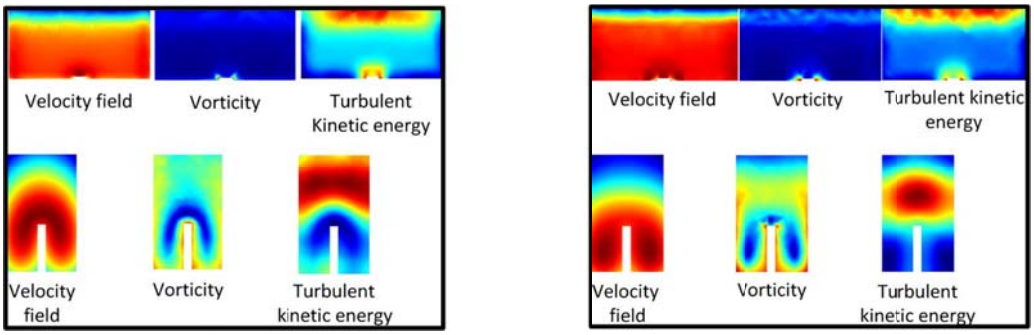

Fig. 24. Aerodynamic performance at the inlet and outlet of a 320 mm (left) and a 160 mm (right) transition with an inlet velocity of 0.1 m/s.

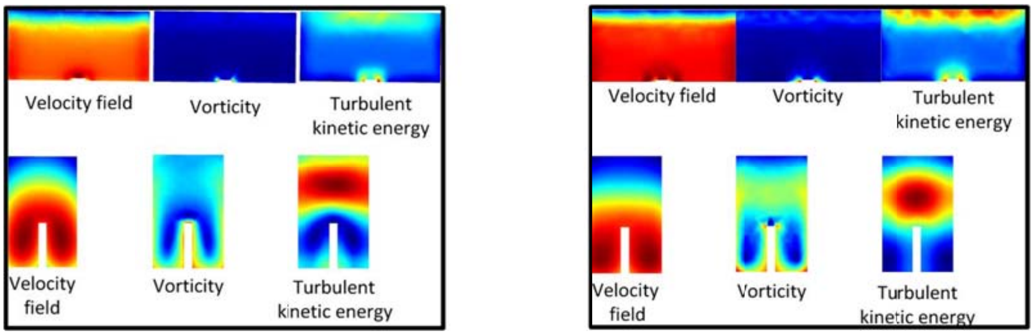

Fig. 25. Aerodynamic performance at the inlet and outlet of a 320 mm (left) and 160 mm (right) long transition with an inlet velocity of 1 m/s.

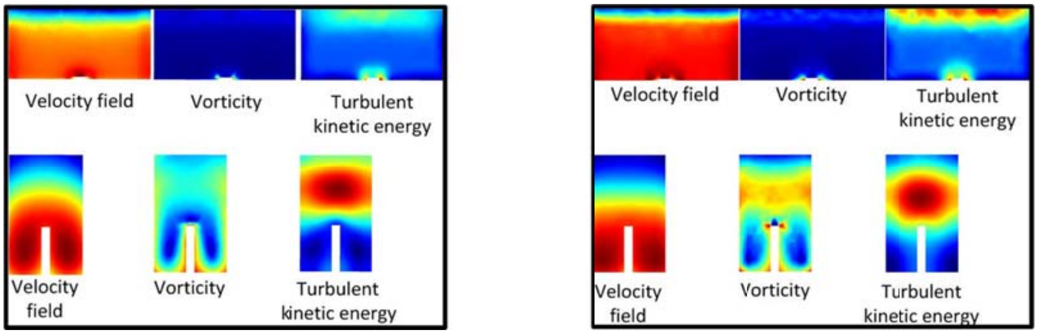

Fig. 26. Aerodynamic performance at the inlet and outlet of a 320 mm (left) and a 160 mm (right) long transition with an inlet velocity of 10 m/s.

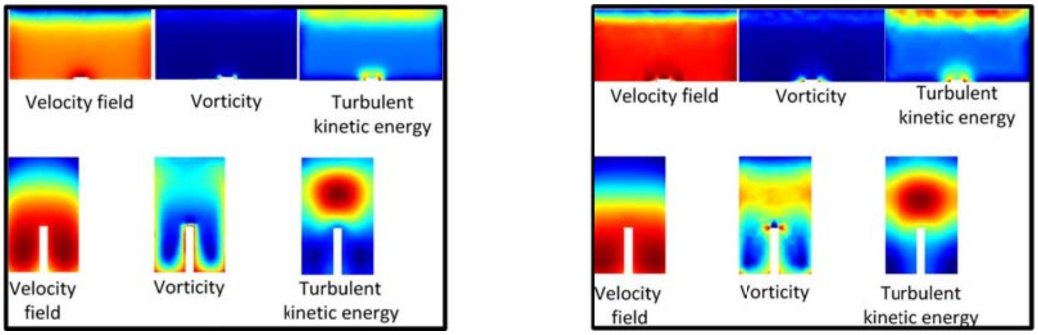

Fig. 27. Aerodynamic performance at the inlet and outlet of a 320 mm (left) and a 160 mm (right) long transitions with an inlet velocity of 25 m/s.

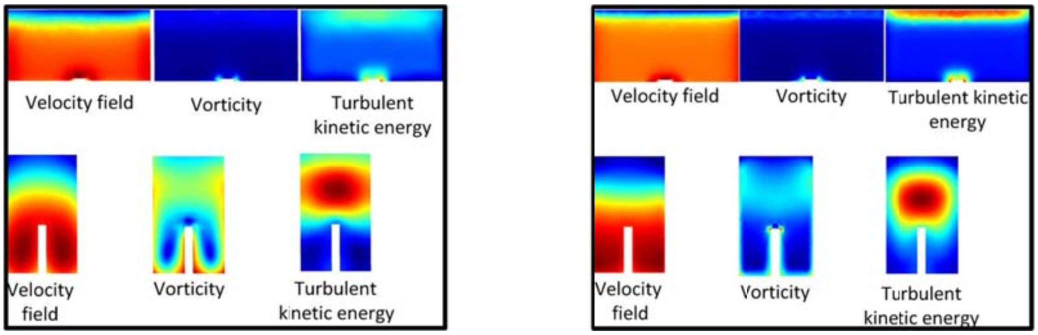

Fig. 28. Aerodynamic performance at the inlet and outlet of a 320 mm (left) and a 160 mm (right) long transition with an inlet velocity of 44.5 m/s.

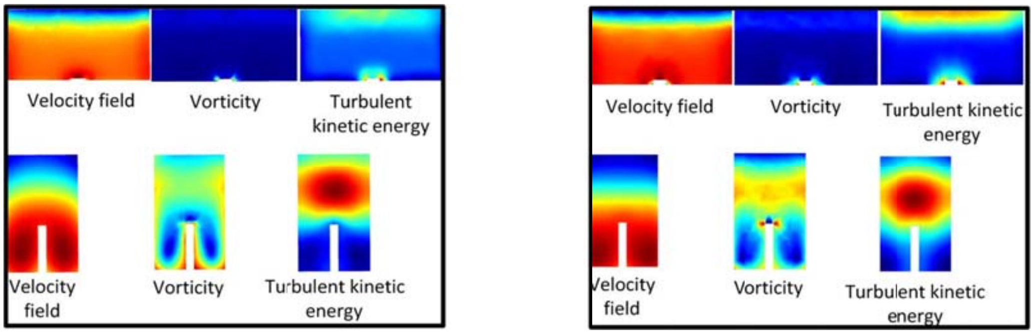

Fig. 29. Aerodynamic performance at the inlet and outlet of a 320 mm (left) and a 160 mm (right) long transition with an inlet velocity of 61 m/s.

The airflow from the RWG-to-TWG transition appears to be more consistent across a wider range of inlet velocities in the long transition by observing the results in Figs. 24-29. These plots show that the air vorticity and velocity are identical at the RWG inlet of the transition, but the TWG outlet of the structure differs. Specifically, the vorticity and velocity plots indicate that the longer transition creates more turbulence and air 'circulation' in the area between the center fin and the sidewalls. This is desirable and justifies the choice of a longer transition. Fig. 30 presents a comparison of the vorticity field at the outlet of the transition to highlight these differences. This scenario will change for different waveguide bands, but this design will function across many cellular networks so the analysis is valid for these ranges of inlet velocities.

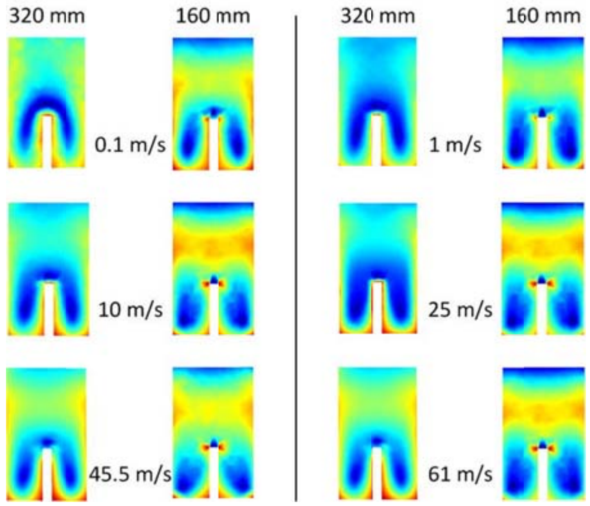

Fig. 30. Vorticity field at the outlet of 320 mm and 160 mm long transitions.

Fig. 31 shows the three dimensional streamline plots of the vorticity vector down the length of the transition. It can be observed from this plot that in the short transition has the stream lines which are not symmetric around the center fin and less dense than the longer transition. In the long transition the vorticity stream lines are symmetric and dense, indicating the presence of turbulences in the troughs and better air 'circulation' in the channel between the center fin and the sidewalls. These results verify that the proposed transition is suitable for applications where broadband reconfigurable radiation from a multifunctional TWG antenna is desired.

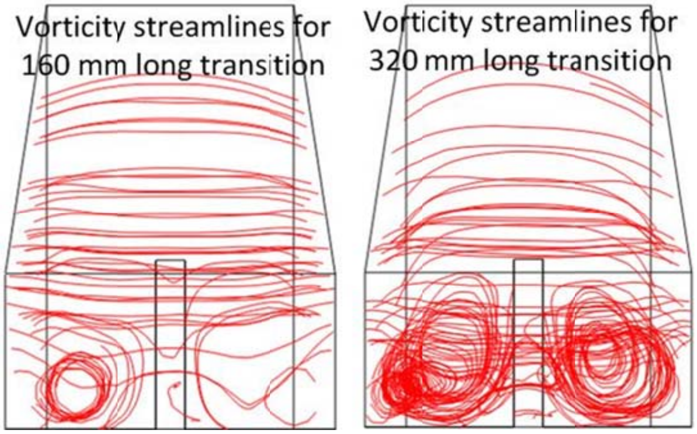

Fig. 31. Streamline plots of the vorticity for a 160 mm and a 320 mm long transition.

CHAPTER IV

A PATTERN RECONFIGURABLE TROUGH WAVEGUIDE ANTENNA

A. Introduction

Metallic blocks were used as perturbations in a TWA for both symmetric and periodically asymmetric leaky-wave antenna designs. These were discussed in Ch. II along with another design that examined the use of vertical and horizontal rods (with a frequency depended length) that were placed atop the center fin to scanned the main beam. This work proposes an alternative electromechanical design using cantilever perturbations in the troughguide; they offer a series of advantages compared with the blocks since they can be made much lighter, are easier to work, and can be functionalized according to the application. They also offer several degrees of freedom that include length for frequency scaling, width for tuning, and angle for amplitude tapering and leakage α from the antenna. Cantilevers can also come in racks as modular component which makes them easily replaceable depending in the requirements of the application. Additionally sensors and other devises can be integrated on the cantilevers for multifunctional operations and potentially can be designed so they can control and be control by air flow without their electromagnetic performance being affected.

B. Simulated Designs

The performance of different cantilever topologies was examined using [11] to better understand the attenuation properties of the cantilever in the TWA. Fig. 32 shows two different configurations, one having the cantilever placed at the junction of the center fin and the bottom plate (case 1) and the other placed at the junction of the side wall and the bottom plate (case 2). Fig. 33 shows the insertion loss per meter as a function of cantilever angle (formed by the cantilever and the bottom plate). This indicates that a cantilever with the same width (24 mm) as the bottom plate, and placed at the junction between the sidewall and the bottom plate, leaks more power per meter especially for angles around 30°.

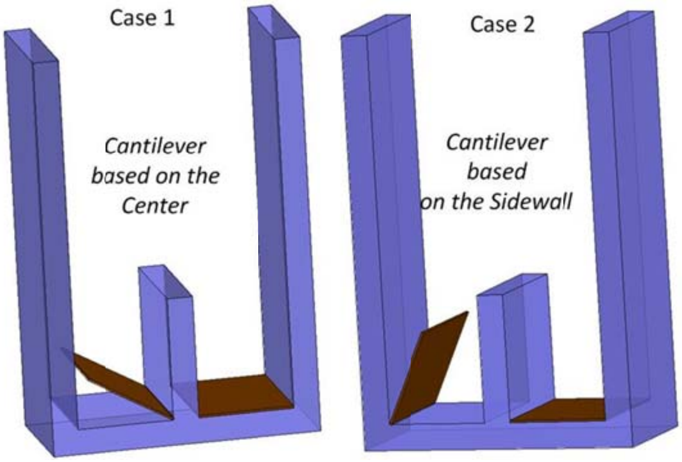

Fig. 32. Cantilever actuated from the center fin (case 1) and from the sidewall (case 2).

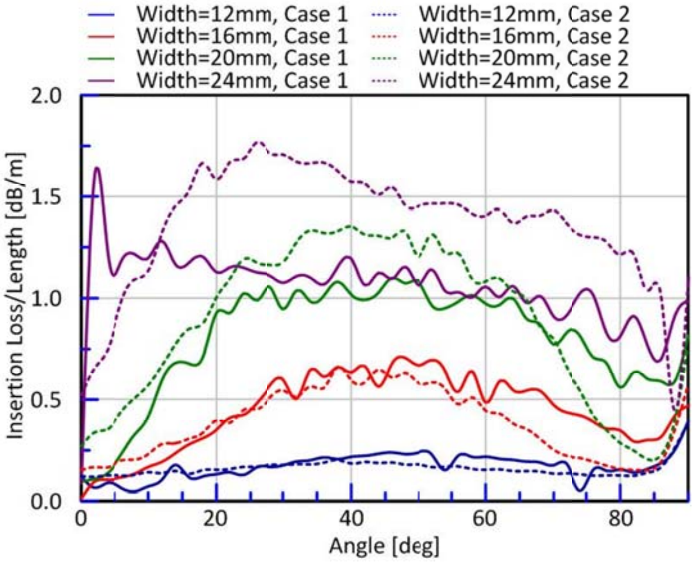

Fig. 33. Insertion loss with respect to the perturbation angle, for cantilevers of different width and placement in the trough.

It is known in antenna theory that the radiation pattern is given by the Fourier transform of the aperture distribution. Tapering the aperture gives control over the radiation pattern and minimizes the side lobe levels, providing at the same time a smoother transition of the fields through the structure. Previous work [7] considered the effect of tapering in radiation and showed that improved radiation patterns are possible (especially away from broadside by tapering the aperture distribution). The cantilevers were not actuated in this fashion for the designs in this work, but the effective aperture was designed for a sinusoidal taper with a 1.2 m long (10λ) effective aperture at 3 GHz.

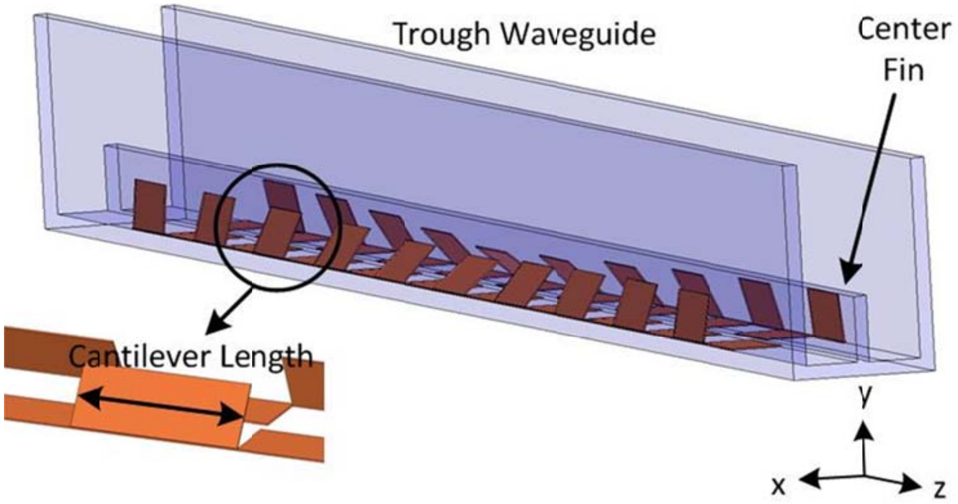

Fig. 34. TWA with cantilever perturbations.

Fig. 35 shows the simulated VSWR and α per unit length (P.U.L.) for cantilever angles varying from 20° to 70° with a 10° step size; this refers to the angle formed by the cantilever pair in the center of the troughguide with the bottom plate (with other cantilevers tapering according to the sinusoidal distribution). For angles less than 50° VSWR has values greater of 2 indicating more than 10% reflection of the delivered power. The VSWR is less than 2 for angles 60° and 70° but as Fig. 35 (right) shows, the radiation only provides $\alpha < 5$ dB/m at 3 GHz (e.g., less than 33% of the input power is leaked). The high VSWR close to 3 GHz is a result of phase accumulation, which occurs at broadside where the cantilevers are half wavelength long (explained in Ch. II). Fig. 36 shows the simulated radiation patterns at 2.6 GHz, 3 GHz and 3.9 GHz with the perturbation angle fixed at 30°; note that the main beam scans as frequency varies.

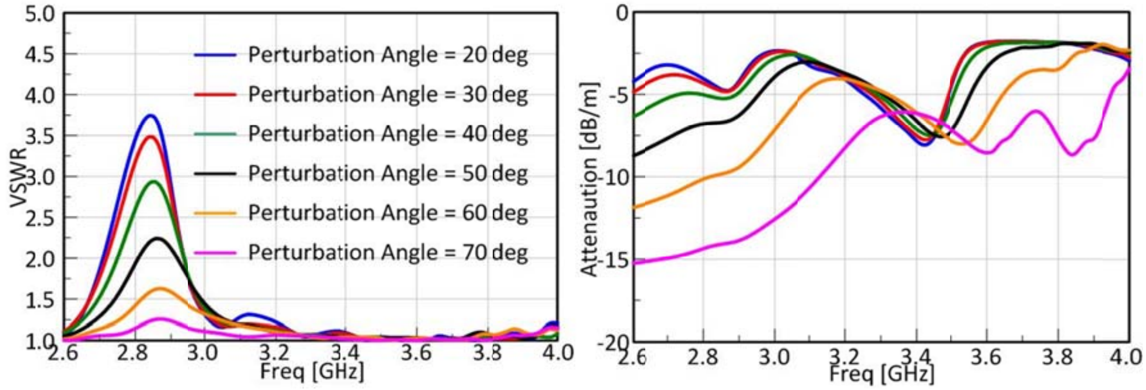

Fig. 35. VSWR (left) and α (right) along the S-band.

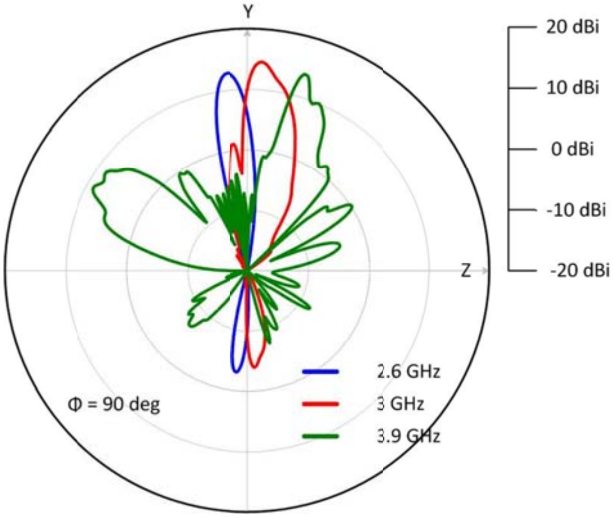

Fig. 36. Radiations patterns, with fixed perturbation angle at 30° and a frequency sweep.

C. Holes in the Center

Arrays of holes, teeth and vertical rods on top of the center fin are two of the methods used in the past to treat high reflections due to phase accumulation. This occurs at broadside-where phase reversal between successive elements is required (common to periodic leaky-wave antennas), which happens in this design in the neighborhood of 3 GHz. Instead of altering the physical structure of the troughguide by making holes on the fin or the walls, holes were designed on the center of each actuated cantilever. Notionally, the cantilevers inside the TWG present a shunt capacitive reactance to the guided wave. This creates reflections due to the cascaded impedance mismatch from successive cantilevers. The circular holes add a shunt inductive reactive to compensate for this effect, and are of interest to this work.

Circular holes of 6 mm and 10 mm diameter were designed on the center of each cantilever as shown in Fig. 37 to provide a compensating effect and educe the impedance mismatch from phase accumulation. Figs. 38 and 39 show the VSWR (left) and α (right) for 6 mm and 10 mm radius holes, respectively, in the center. Although both designs showed improvement to the VSWR – bringing it from a VSWR = 3.5 (with no holes) to a VSWR = 2.5 (with hole to the center) – but a lower VSWR is required. Taking a closer look at the current distribution produced on the cantilevers in Fig. 37, it can be observed that the currents are stronger at the edge of each cantilever compared to the center. This suggests that the hole should be placed at the edge where it can perturb the current and generate a higher inductive loading.

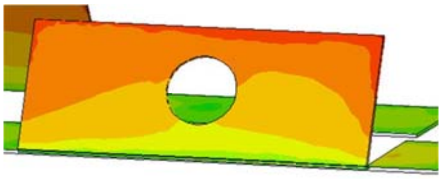

Fig. 37. Currents excited on a cantilever with a hole in the center.

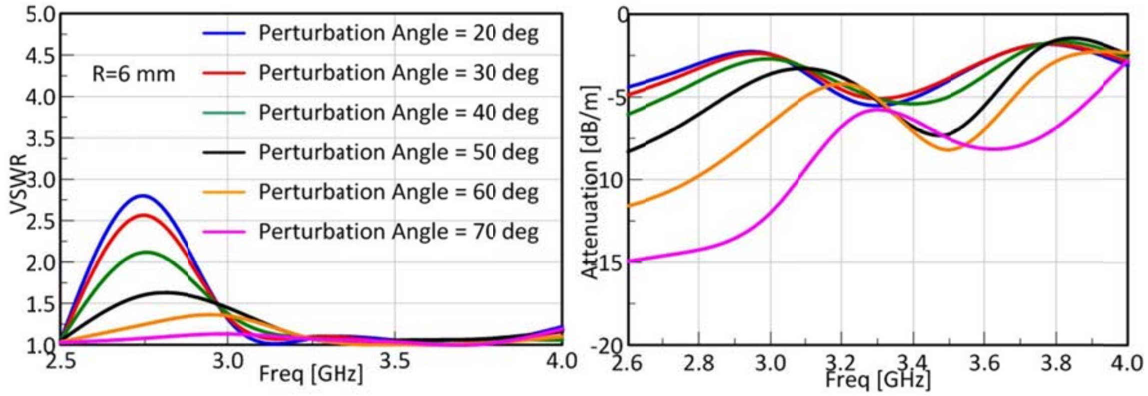

Fig. 38. VSWR (left) and α (right) for cantilevers with a 6 mm radius hole on the center.

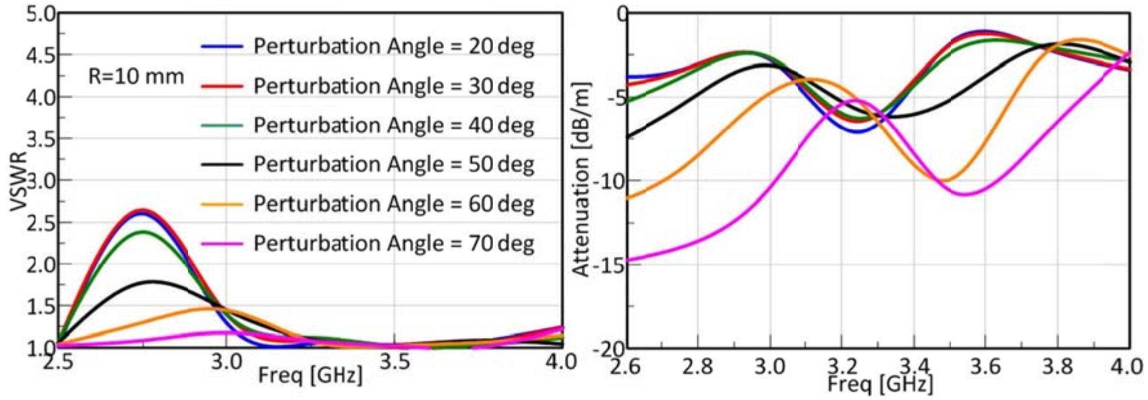

Fig. 39. VSWR (left) and α (right) for cantilevers with a 10 mm radius hole on the center.

D. Holes at the Edge

The design in Fig. 37 was modified so each hole moved beyond the outer edge of each cantilever (Fig. 40); this was based on that observation of current density on the cantilever. Figs. 41 and 42 show the VSWR (left) and α (right) for the modified design with one hole of radius of 6 mm and 10 mm at the edge of each cantilever respectively. These plots indicate that the VSWR was reduced below 2 (especially the 6 mm radius) for a 30° perturbation angle with more than 50% of the total power lost per meter.

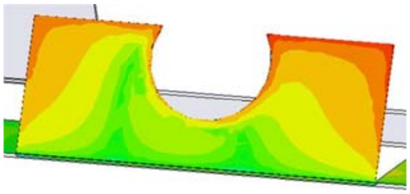

Fig. 40. Currents excited on a cantilever with a hole at the edge.

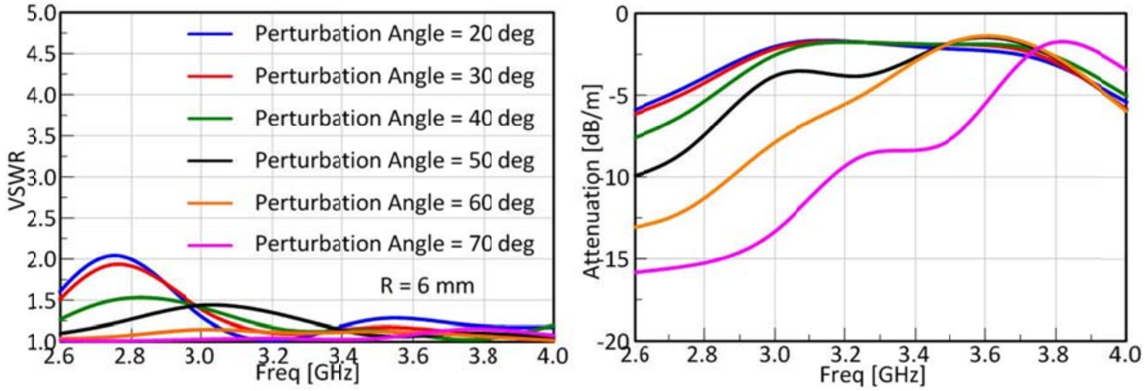

Fig. 41. VSWR (left) and α (right) for cantilevers with a 6 mm radius hole at the edge.

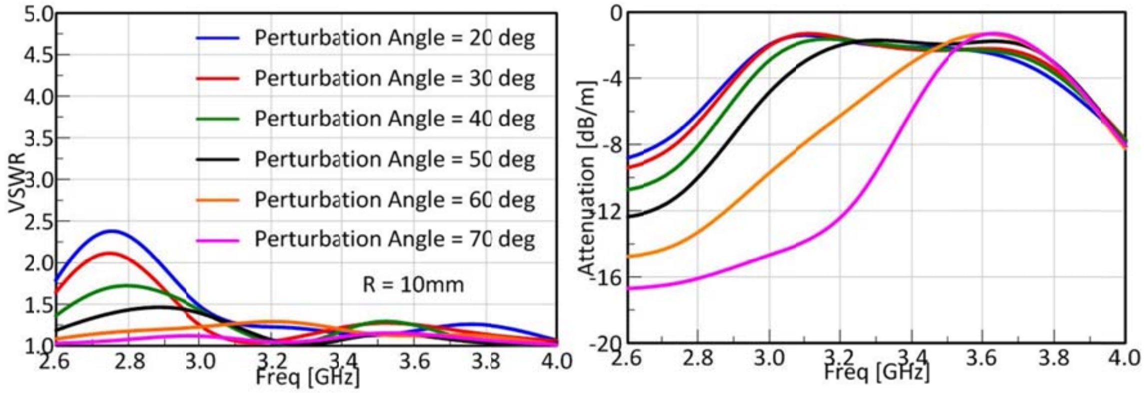

Fig. 42. VSWR (left) and α (right) for cantilevers with 10 mm radius hole at the edge.

Designs with holes of 6 mm and 10 mm radius at the center and the edge of the cantilever are compared in Fig. 43 for a perturbation angle of 30° showing the improvement in VSWR when the hole is moved towards the edge. Cantilevers with holes at the edge appear to be electrically longer at the operating frequency (> $\lambda_0/2$) compared to the cantilevers without holes, but phase accumulation does not cause a high reflection coefficient near the frequency with broadside radiation. The radiation properties of the antenna are not affected, providing a narrow beam at broadside region.

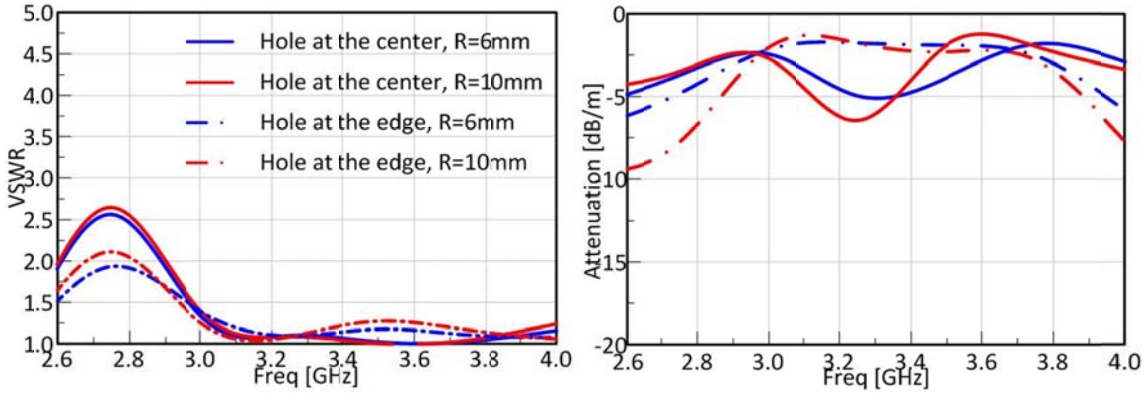

Fig. 43. VSWR (left) and α (right) for cantilevers with edge and center holes with a 30° angle.

E. Cantilevers with Two Holes

A design with two holes on each cantilever (6 mm and 8 mm radii) is shown in Fig. 44. This was examined to observe the impact of a more significant perturbation on the current and its effect on the VSWR and radiation patterns. The results for two designs with identical 6 mm and 8 mm radii holes are plotted in Fig. 45 for a fixed perturbation angle of 30°. The VSWR is lower than 1.5 for perturbation angle of 30° when the holes have a radius of 6 mm. Radiation patterns as shown in Fig. 46 for the dual-hole design with 6 mm, 8 mm and 10 mm holes (on each cantilever); no pattern deterioration is apparent and the main beam points towards near broadside.

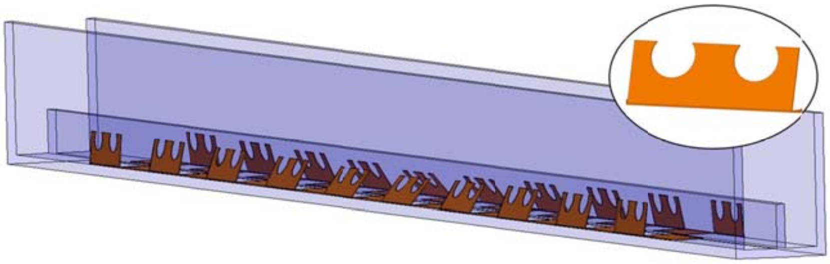

Fig. 44. TWA with two holes on each cantilever.

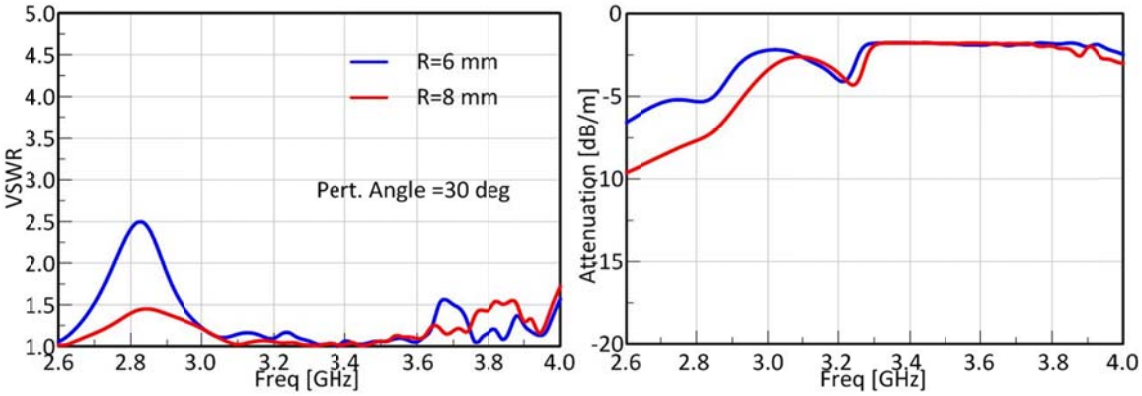

Fig. 45. VSWR (left) and α (right) for cantilevers with 6 mm and 8 mm radius holes and 30° perturbation angle.

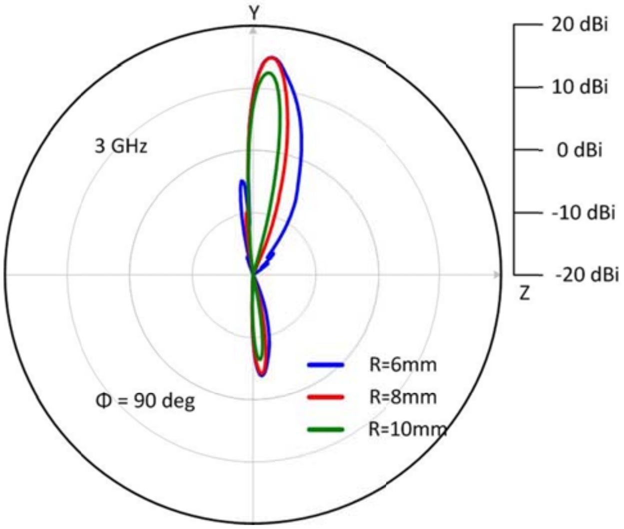

Fig. 46. Radiation patterns for a TWA with cantilevers with two holes of 6 mm, 8 mm and 10 mm.

F. Different Matching Geometries

The effect of holes with triangular and rectangular geometries was also examined for two- and three-hole designs (e.g., holes per cantilever). This is shown in Fig. 47. Similar results were observed, showing a reduction to the VSWR and effectively mitigating the high reflections due to phase accumulation. Radiation patterns do not deteriorate significantly at the center of the band (as desired) and there is only a nominal change in the main beam's beam direction. The VSWR of all three geometries (with and without two holes on each cantilever) is shown in Fig. 48 for a 30° perturbation angle.

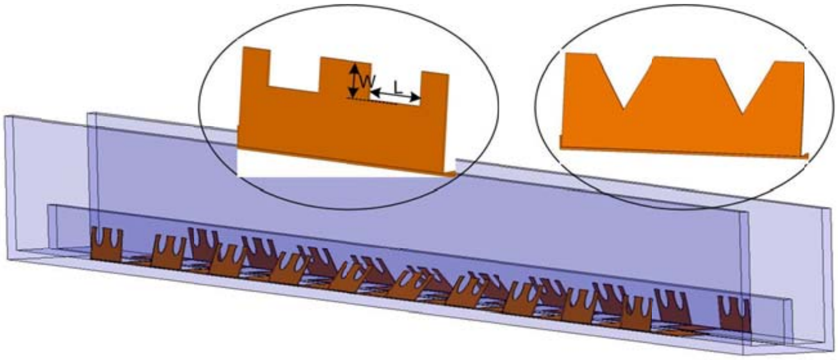

Fig. 47. TWA with two triangular or rectangular holes.

All three cases provided in Fig. 48 show a VSWR < 2; however, the circular and rectangular geometries generally treat the problem more effectively. Three–hole designs for the circular, triangular, rectangular topologies on each cantilever were also examined and showed an even greater effect towards reducing the VSWR

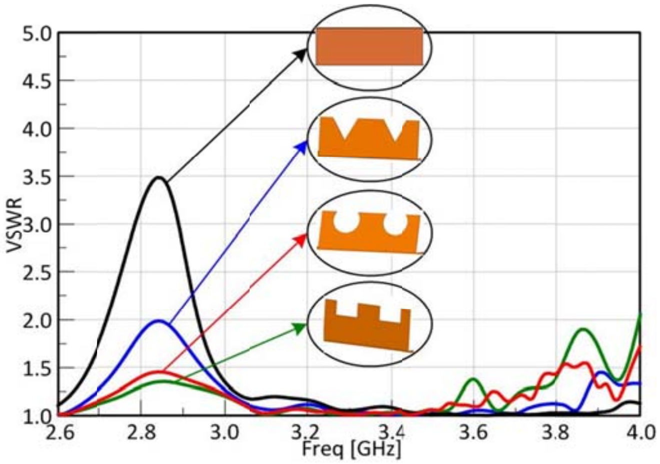

Fig. 48. VSWR of the TWA with two holes of circular, triangular and rectangular geometries.

G. Fabrication of the TWA

Two pieces of TWA were fabricated from 1/4 inch thick aluminum plates. Each wall was milled and tapped accordingly for construction using machine screws. The dimensions of the structure are b_2=54.35 mm, a_2 = 93 mm, t = 6.35 mm, and h=37 mm as explained in Fig. 49. Each piece was 75 cm long as it was the maximum length that the milling machine could process providing an overall aperture 1.5 m long. Custom flanges were also designed and fabricated to connect the two pieces together and mount the transitions and the feed connections to the troughguide. Figs. 50 and 51 show the CAD drawings of the parts used to fabricate the TWG and shown where screw holes are located.

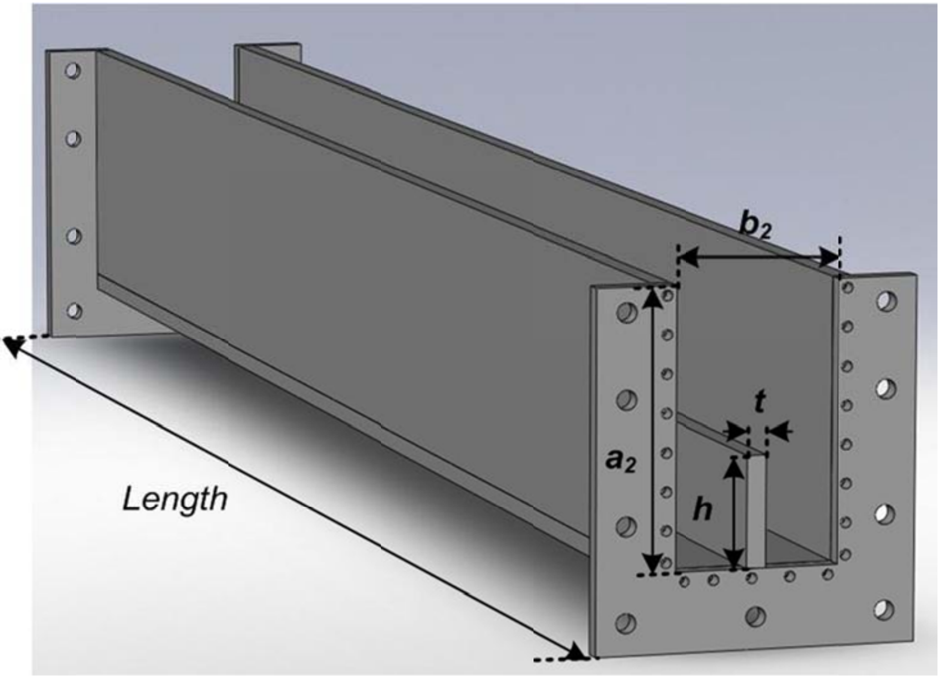

Fig. 49. CAD design of the trough wave guide.

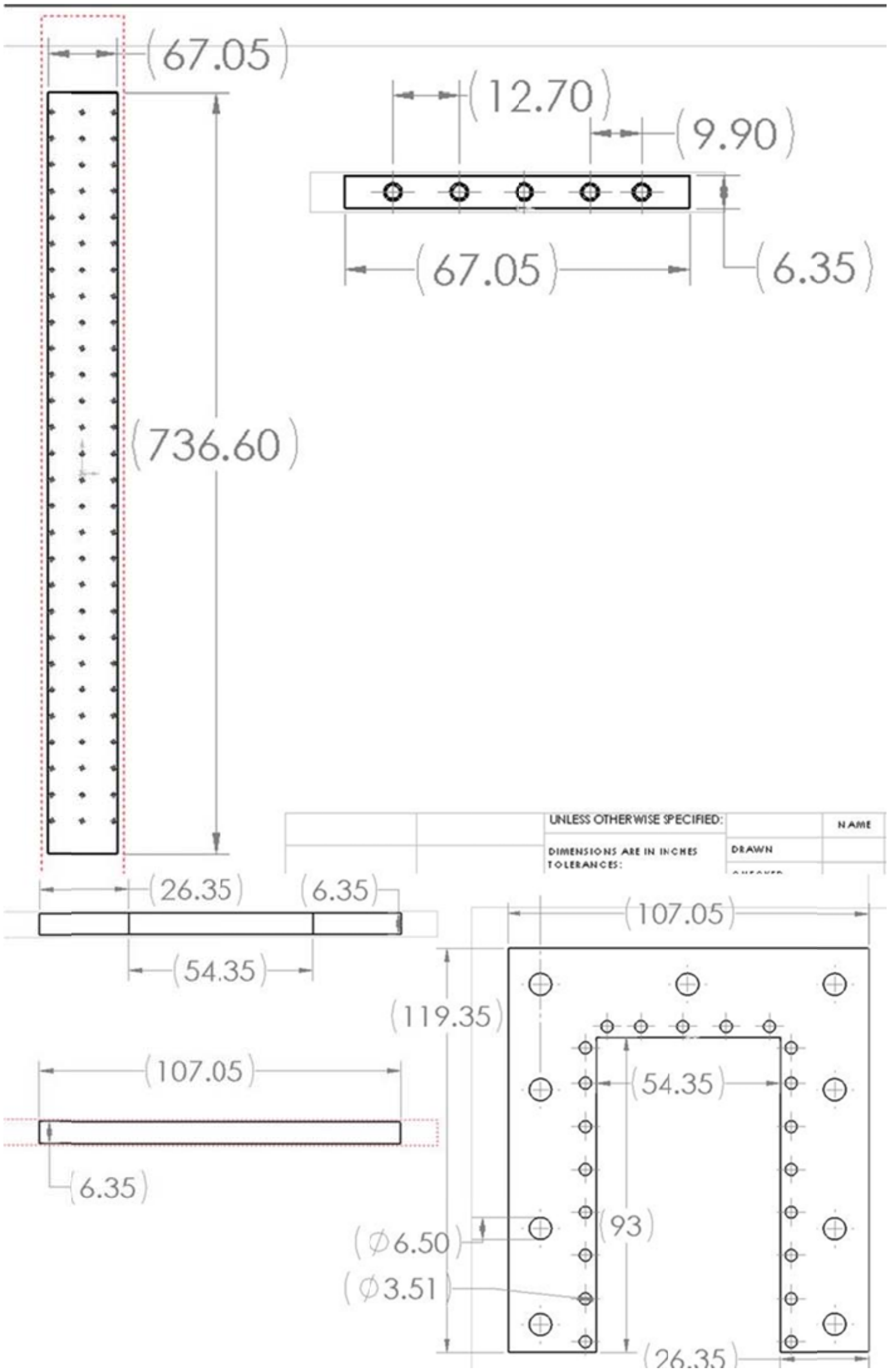

Fig. 50. CAD drawing of the bottom plate of the troughguide (upper) and the custom made flange (lower).

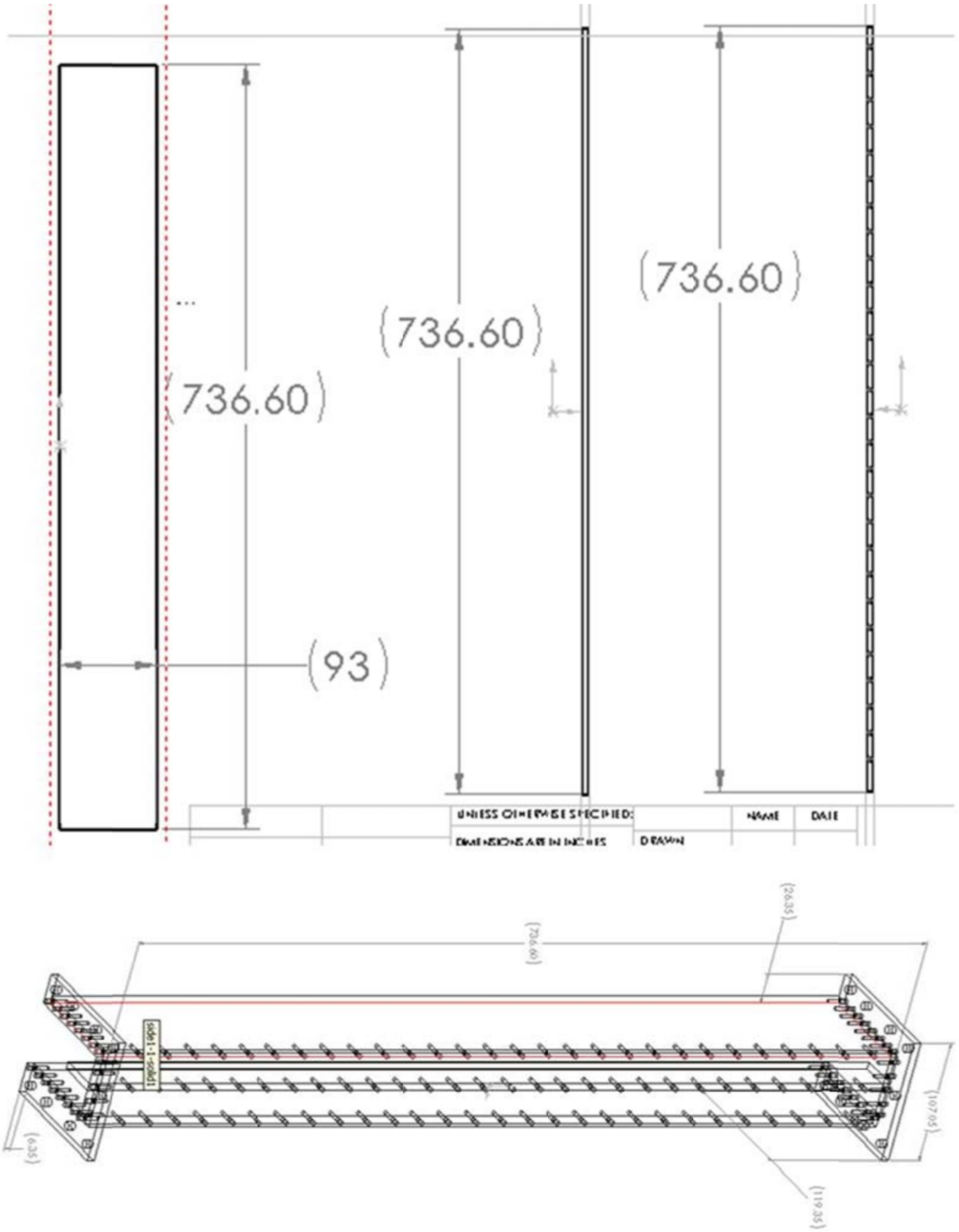

Fig. 51. CAD drawings of the troughguide.

H. Experimental Setup I

Two sets of cantilevers were fabricated according to the previous results; these were made from 0.6 mm thick copper sheets. Each set had four 60 cm long racks (due to the dimensions of the metal sheets) giving a 1.2 m (10λ) long aperture. Each rack has a 2 mm base in order for mechanical stability at the bottom of the TWA. The width of the cantilevers is 22 mm (e.g., 2mm less than the width of the trough) and each has the length of 60 mm for broadside radiation near 3 GHz. The fabricated version without holes can be seen on the left of Fig. 52. The transitions were placed into the TWA and measured using an Agilent Technologies E8361C network analyzer that was calibrated with an S-Band waveguide calibration kit. The VSWR is shown on the right side of Fig. 52, and Fig. 53 shows the radiation patterns for both the co-polarization and cross-polarization patterns at 2.6 GHz, 3 GHz, and 3.9 GHz. Measured results are in no agreement with the simulated results for this configuration. This deviation was due primarily to fabrication errors in machining the cantilevers (not of all of the same exact length and width). Some cantilevers were also forced into the structure and deformed. This created air gaps between the troughguide walls and the cantilevers. A second set of cantilevers was made with a hole at the edge but it was not tested.

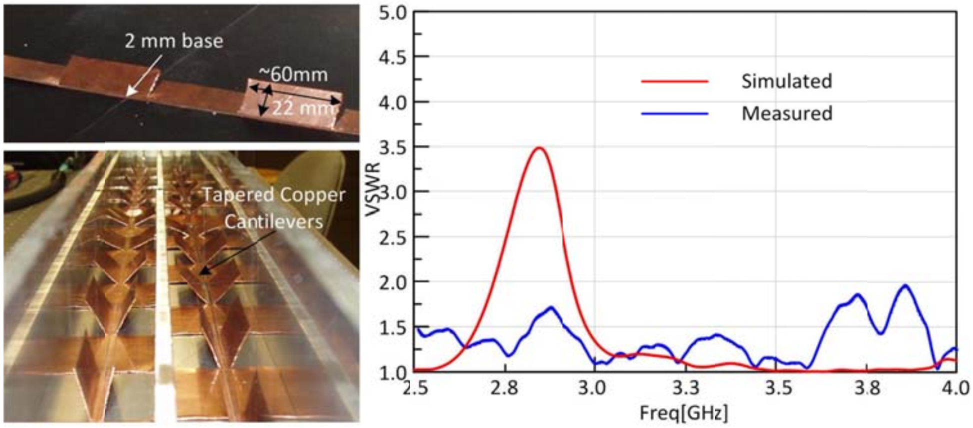

Fig. 52. Fabricated version of cantilevers for broadside radiation using copper sheets (upper left), Copper cantilevers placed in the TWG (lower left), measured and simulated VSWR.

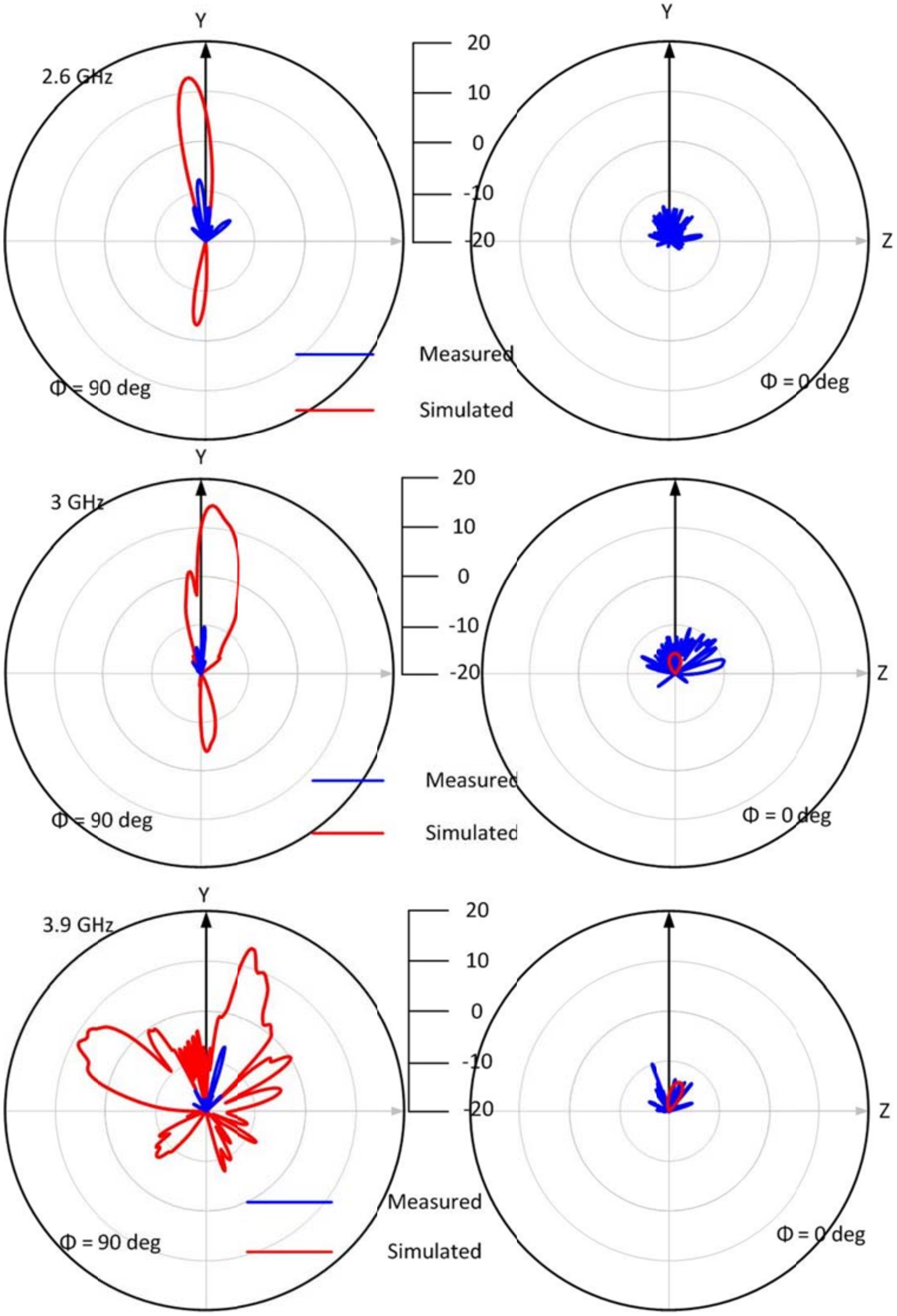

Fig. 53. Radiation patterns at 2.6 GHz, 3 GHz, and 3.9 GHz at the co-polarization and cross-polarization planes.

I. Experimental Setup II

The fabrication difficulties and sensitivity of the TWA to the cantilever dimensions provided many lessons-learned, so an alternative approach was developed for the same design using copper tape on paper cantilevers. This gave more control for hand fabrication. The main deviation from the previous design is that the width of each cantilever is now able to be 24 mm (the full width of the trough) since no base is needed for mechanical support. The copper tape also has thickness of 0.025 mm instead of 0.6 mm. An aperture 120 cm (10λ) long was formed using 20 actuated copper cantilevers taped on paperboard. Two sets were made, one without holes (Fig. 54, lower right) and one with a single hole at the edge of each cantilever (Fig. 54, upper right); the paper cantilevers inside the troughguide are shown in Fig. 54.

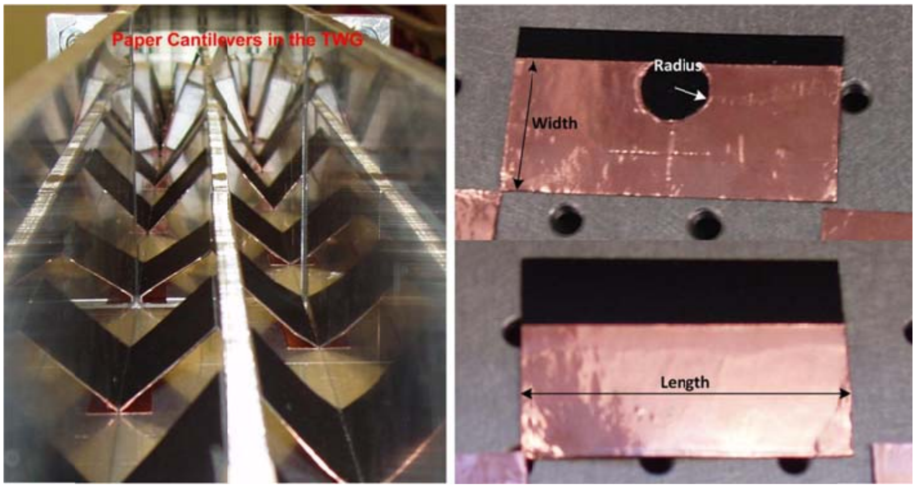

Fig. 54. Fabricated cantilevers in the TWG (left), λ/2 paper cantilever with one hole (upper right), λ/2 paper cantilever with no hole (lower right).

The paper cardstock was marked using a caliper and cut using a guillotine-style paper cutter. A piece of copper tape was placed on each card. For better electrical contact it was taped against the bottom wall of the troughguide (the tape has a conductive adhesive). The angle of these paper cantilevers was tapered in a sinusoidal manner starting from the center of the guide towards the ends. Small pieces of foam were used to support the cantilevers to the right angle. After measuring the structure the cantilevers were taken out and a hole, 12 mm in diameter, was cut on every one using a razor blade.

1. λ/2 Cantilevers with No Holes

Half-wavelength cantilevers (at 3 GHz) were placed in the TWG and the performance of the antenna was measured using a network analyzer. The VSWR plots in Fig. 55 (left) show the spike in VSWR (due to phase accumulation) close to the operating frequency at both simulated and measured results. Insertion loss plots in Fig. 55 (right) indicate that 90% power was attenuated via radiation through the aperture. Radiation pattern measurements in the anechoic chamber also indicate agreement between the simulated and measured results (co- and cross-polarization) at 2.6 GHz, 3 GHz and 3.9 GHz (Fig. 56). An antenna gain G near 14 dBi was achieved at broadside.

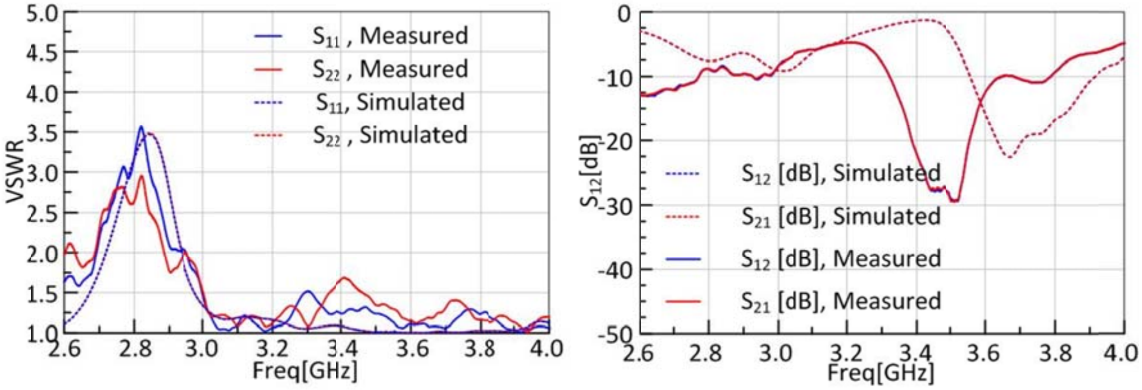

Fig. 55. Measured and simulated insertion loss (left), VSWR (right).

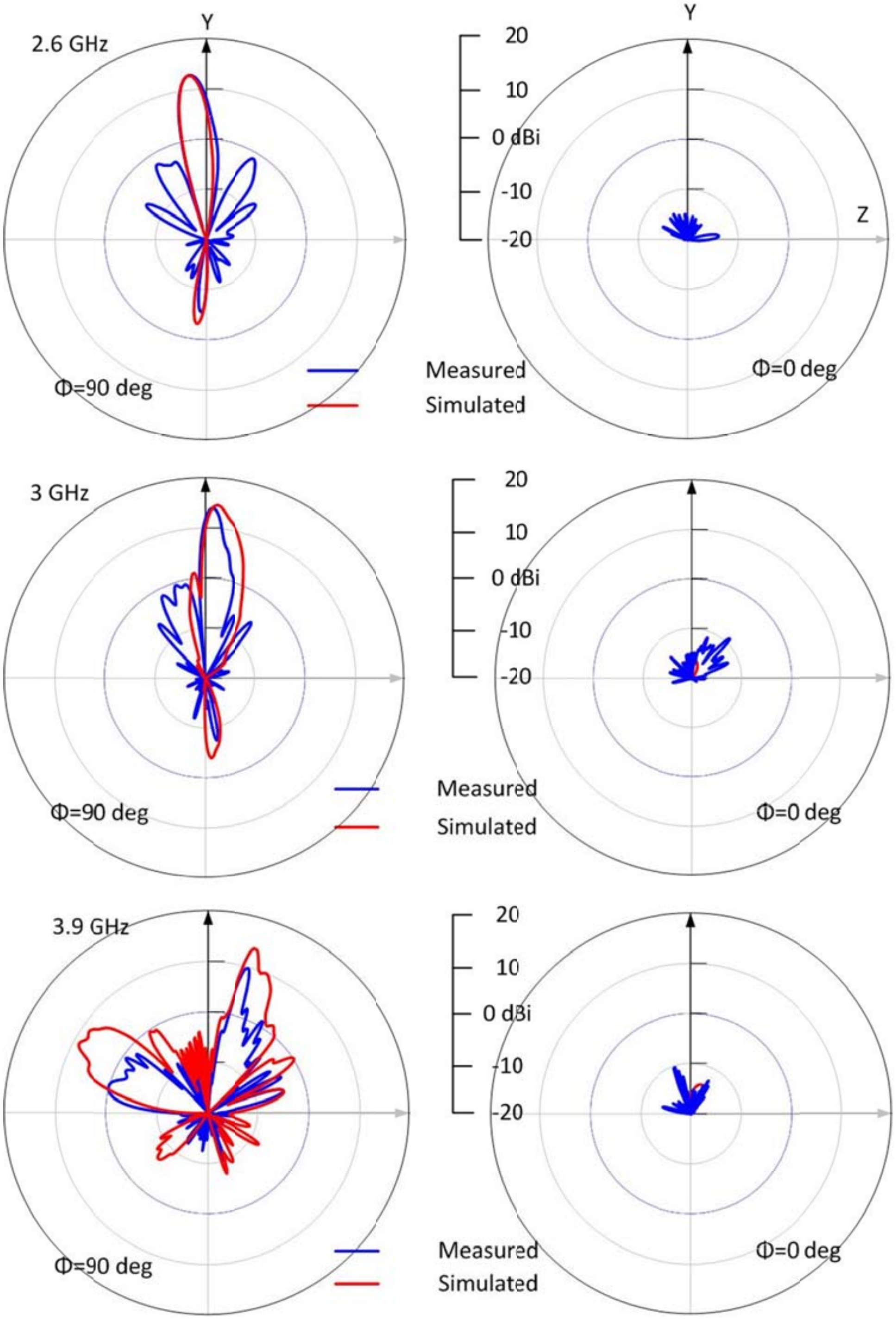

Fig. 56. Co- and cross-polarization plane radiation patterns of the TWA with cantilevers.

2. λ/2 Cantilevers with a Hole

Prior results showed that reflections due to phase accumulation can be reduced by cutting holes at the edge of each cantilever. Half-wavelength cantilevers with a 6 mm radius hole at the edge were placed in the TWG providing a 120 cm (10λ) long tapered aperture. The VSWR was measured and plotted against frequency along with the simulated data as seen in Fig. 57 (left). It is seen that the VSWR was lowered, as expected, but the peak was shifted to the left (a lower frequency) as the holes on each cantilever were not identical and were roughed out of the copper tape, resulting in asymmetries. Moreover, most of the holes were measured to have a larger radius than the design making the cantilever to appear longer, which explains the frequency shift. The insertion loss plotted at Fig.57 (right) appears also shifted for the same reasons.

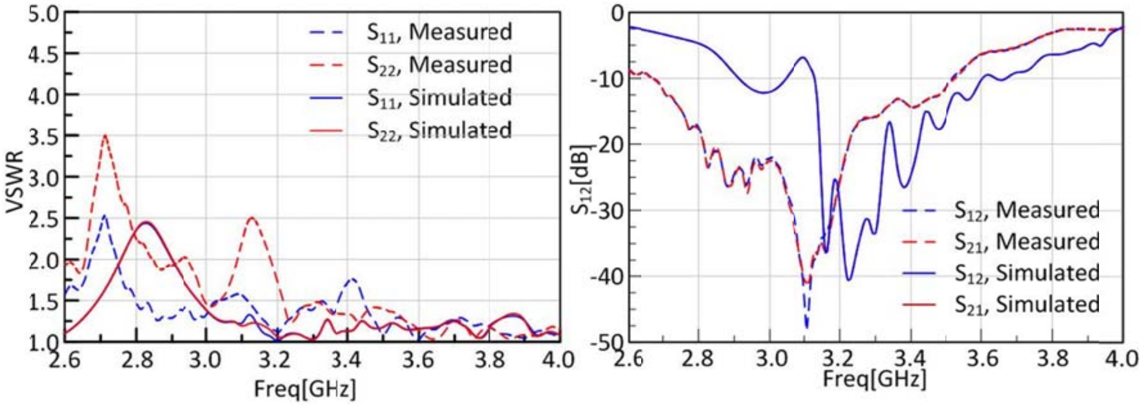

Fig. 57. Measured and simulated VSWR (left) and insertion loss (right).

In Fig. 58 is a picture of the experimental setup inside the anechoic chamber. The trough waveguide antenna is mounted on a rotating stand across the standard antenna. Fig. 59 shows the radiation patterns for the half wavelength cantilevers with one hole at the edge for both the co- and cross-polarization at 2.6 GHz, 3 GHz and 3.9 GHz. Measured and simulated results are in agreement and capture the main beam steering with frequency. Measured results show much higher sidelobes compared to the simulation but this is attributed to fabrication difficulties. The aperture was also not tapered accurately and a result is the appearance of high level sidelobes.

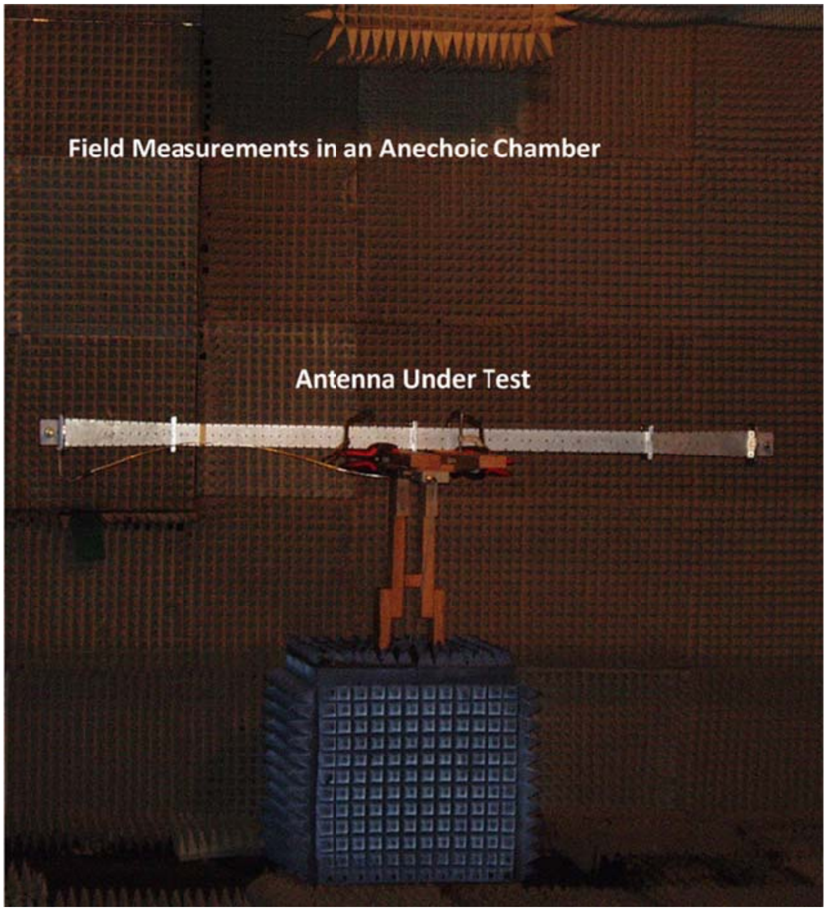

Fig. 58. Experimental setup for measuring radiation patterns in the anechoic chamber.

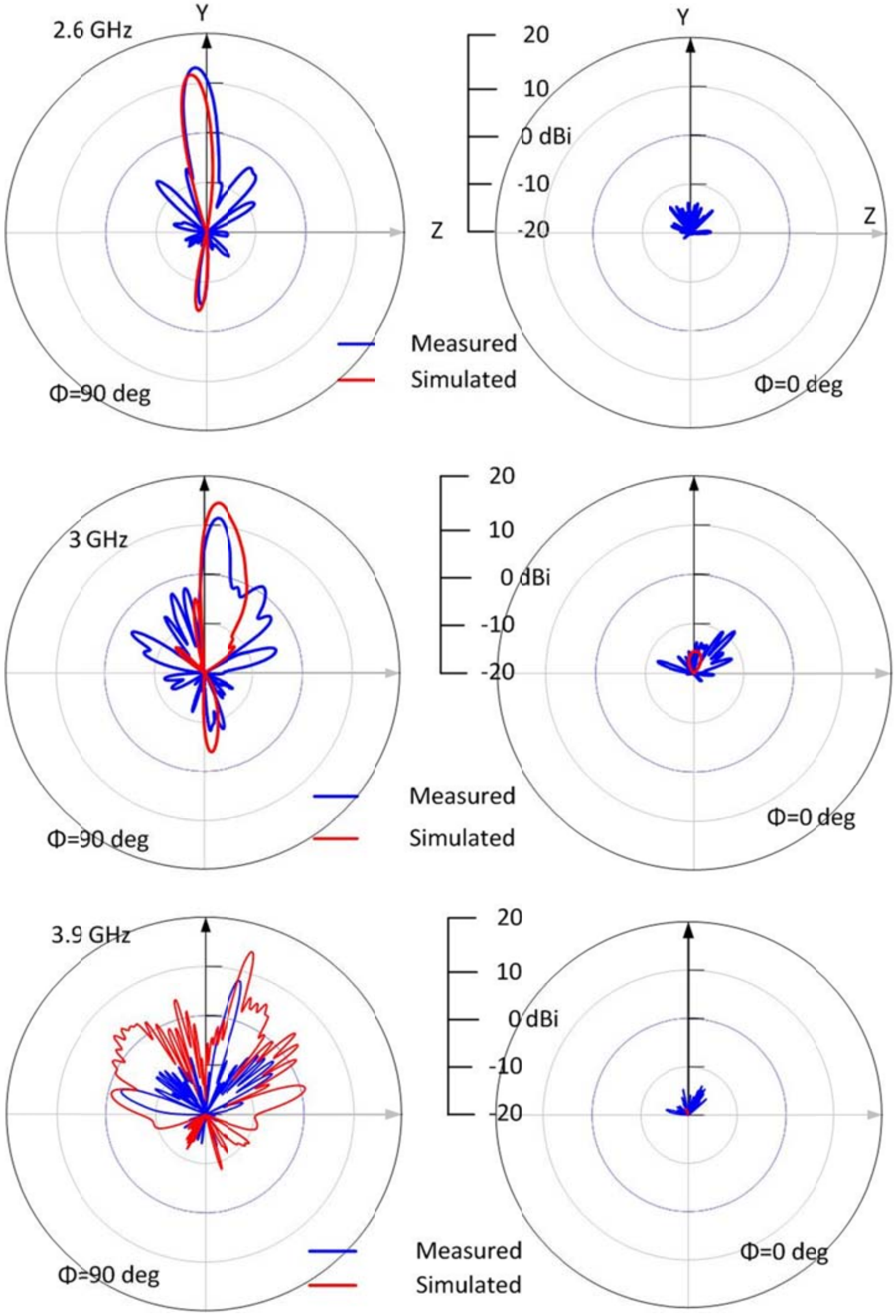

Fig. 59. Radiation patterns for the half wavelength cantilevers with a hole.

J. Experimental setup III - Pattern Reconfigurable Design

Reconfiguration of the radiation pattern at a fixed frequency was evaluated in the third setup using quarter wavelength long cantilevers that were simulated and fabricated with copper tape on car-stock paper – this was done both with and without holes. The cantilevers were actuated with a distribution given by a cosine amplitude distribution (30) about the center of the TWA. Fig. 60 shows the perturbation angle of each cantilever corresponding to the amplitude distribution starting from one end to the middle of the troughguide. The angles are shown for 12 cantilevers, which form an aperture of 144 cm in total from one end to the other, with the middle having the strongest perturbations-bigger angles. In order to consider the effect of the perturbation length and the direction of the beam, cantilevers were actuated one, two, and three at a time in anti-symmetric pairs. Each length (one, two, or three at a time) of cantilever groups corresponded to one-quarter, one-half, and three-quarter wavelength perturbations. Experimental and simulated results follow which illustrate that the TWA with cantilever perturbations can be used for reconfigurable beam steering, scanning form the backward quadrant trough broadside to the forward quadrant.

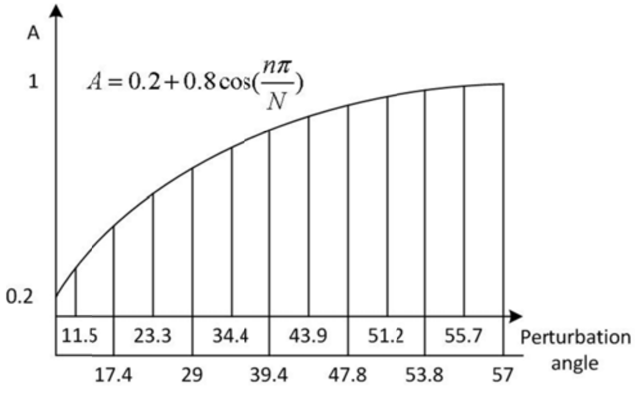

Fig. 60. Tapering perturbation angle for 12 cantilevers form one end to the middle of a TWG.

1. λ/4 Cantilevers

A new set of cantilevers was made using copper tape and paper. Each cantilever was 30 mm ($\lambda/4$) long 24 mm wide as represented at Fig. 61. The cantilevers were placed in the trough waveguide as before taped on the sidewalls, tapered with a cosine distribution given by (30) and supported by small pieces of foam (which are EM transparent due to their electrical permittivity being near unity). In (30) N is the number of cantilevers in half the trough and n corresponds to the index of the n^{th} cantilever from the center. Fig. 62 (left) shows the simulated and measured VSWR. The cantilevers are not a half-wavelength so there is no phase accumulation problem. The measured and simulated S-parameters are potted at Fig. 62 (right). The measured radiation patterns, Fig. 63, show higher sidelobes compared to the simulated mainly because the tapering was made approximately. At 3 GHz the main beam is 50° from broadside towards the backward quadrant.

$$A = 0.2 + 0.8\cos(\frac{n\pi}{N}) \tag{30}$$

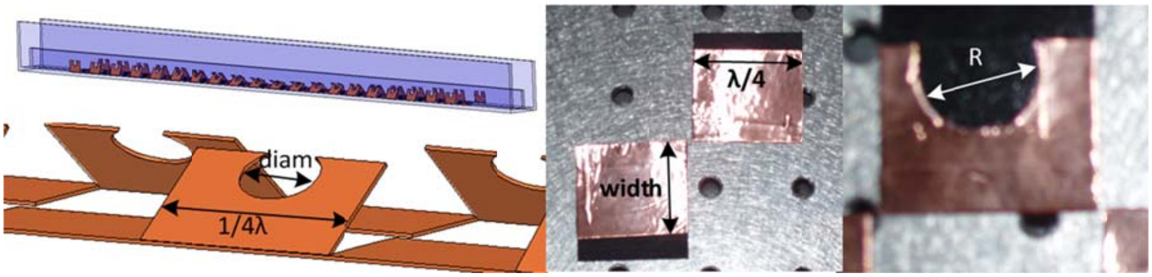

Fig. 61. Quarter wavelength long cantilevers.

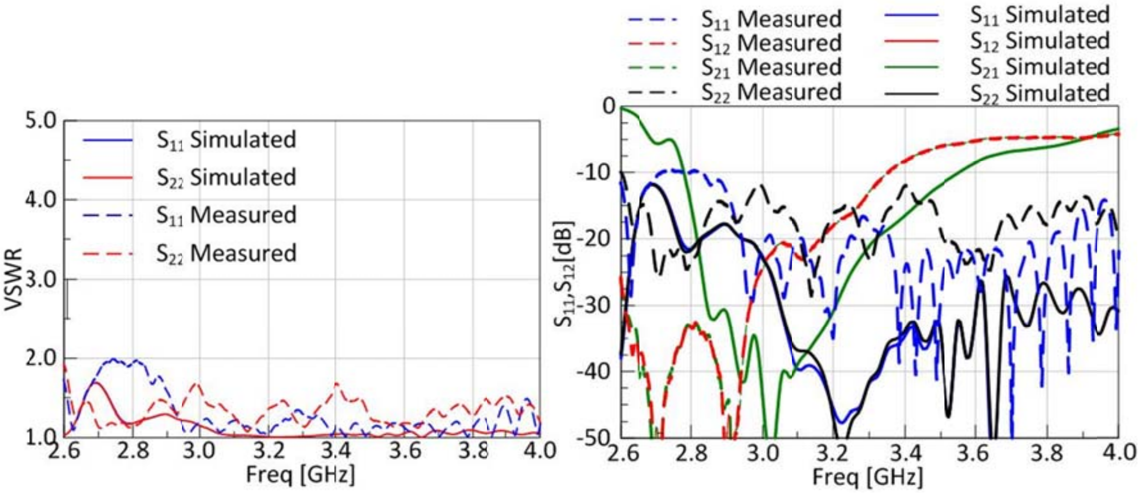

Fig. 62. Measured and simulated VSWR (left) and S-parameters (right).

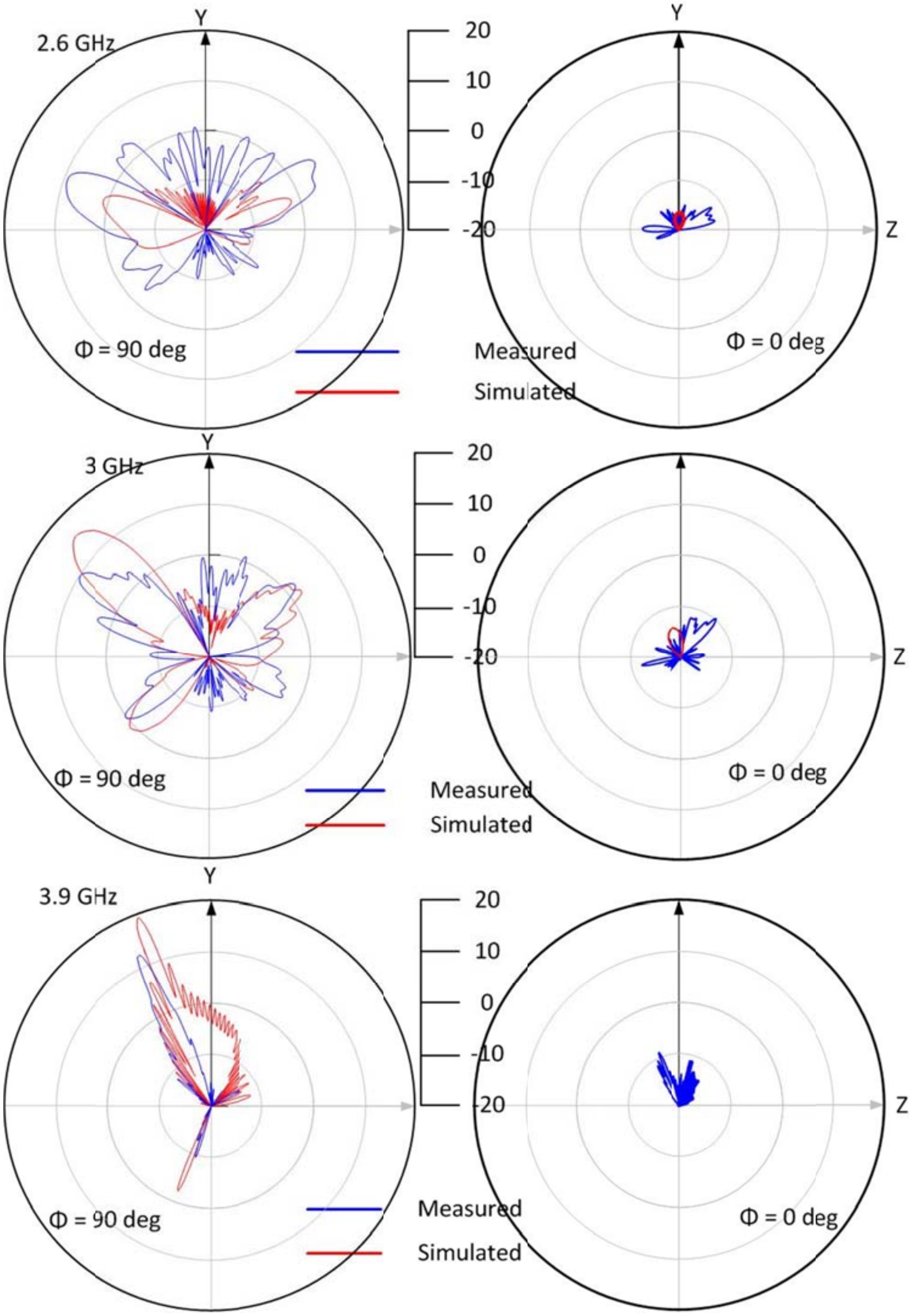

Fig. 63. Radiation patterns at the co-polarization and cross-polarization planes at 2.6 GHz, 3 GHz and 3.9 GHz.

2. λ/4 Cantilevers with a Hole

An 8 mm radius hole was made in each quarter-wavelength cantilever. Figs. 64 show the VSWR (left) and S-parameters in dB (right). The results do not show any phase accumulation. Radiation patterns are displayed at Fig. 65 for the quarter long cantilevers with an 8 mm radius hole. At 3 GHZ measured and simulated results show the main beam pointing 50° away from broadside to the backward quadrant.

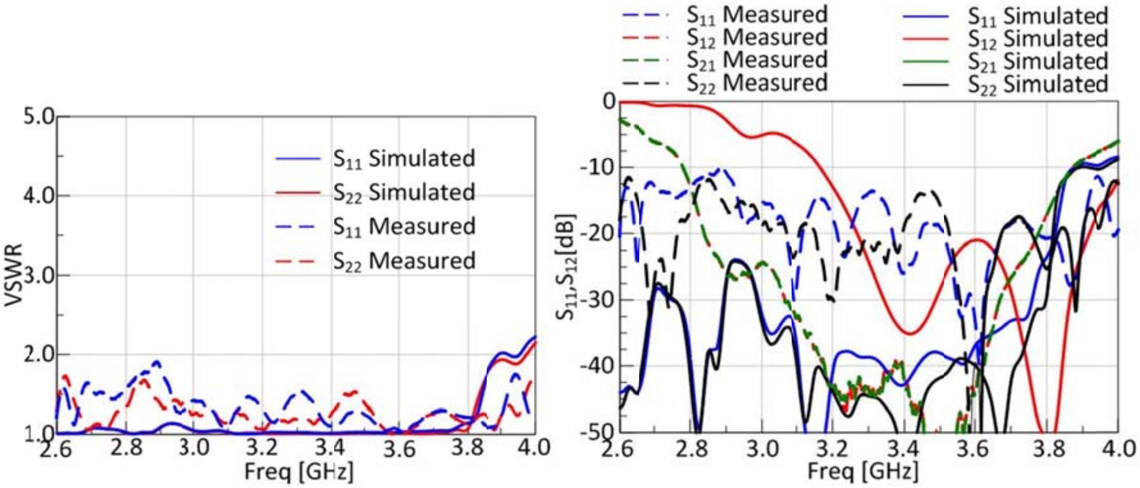

Fig. 64. Measured and simulated VSWR (left) and S-parameters (right).

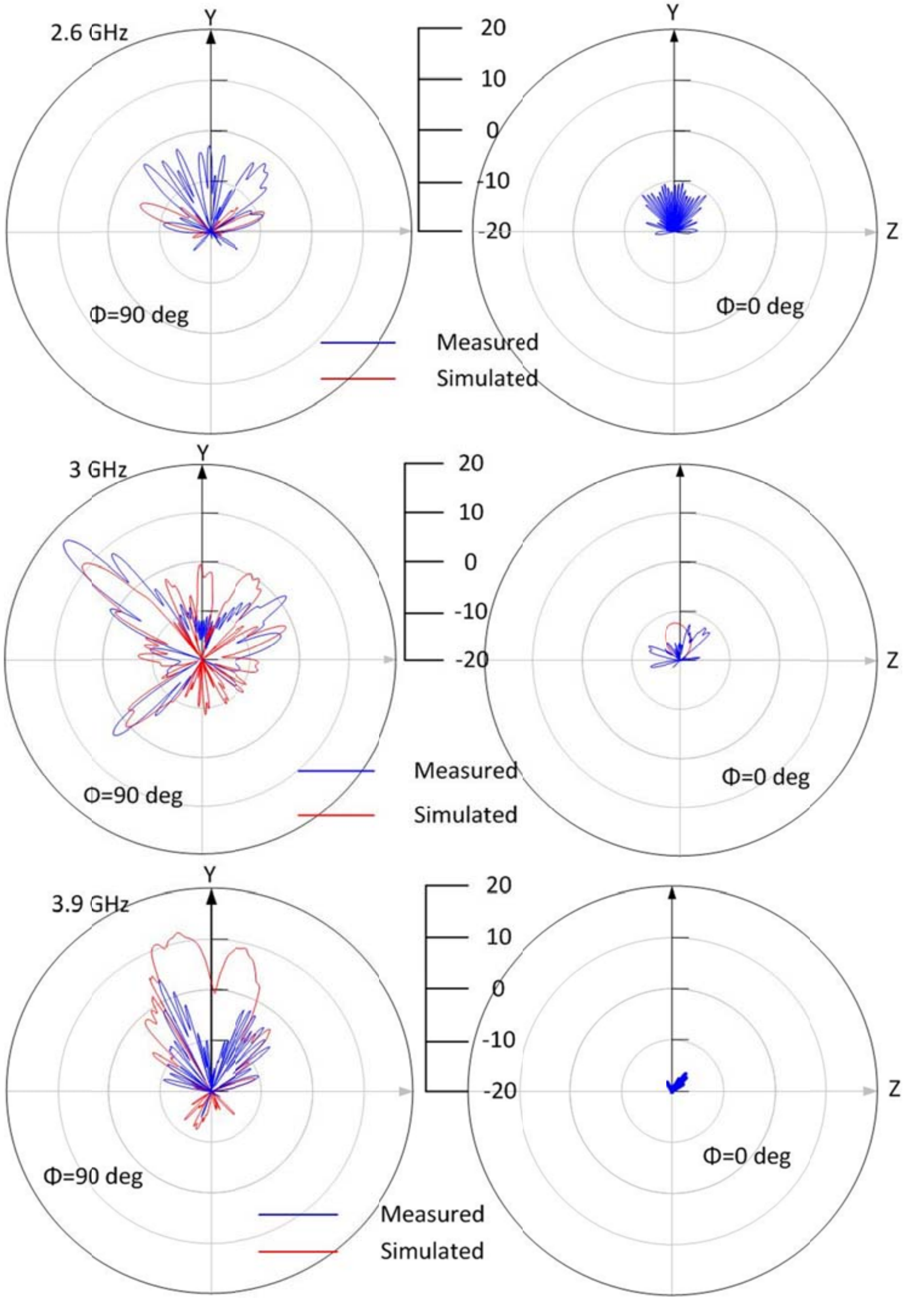

Fig. 65. Radiation patterns at the co-polarization and cross-polarization planes at 2.6 GHz, 3 GHz and 3.9 GHz.

3. *λ/2 Cantilevers*

Two quarter-wave long cantilevers were then actuated together as single perturbation (each at the same angle) to provide a half wave long cantilever. The TWA with half-wave long cantilevers (no holes) was measured and results are shown along with simulated results in Fig. 66. Measured and simulated VSWR (Fig. 66, left) are in good agreement, showing a peak around to 2.9 GHz due to phase accumulation.

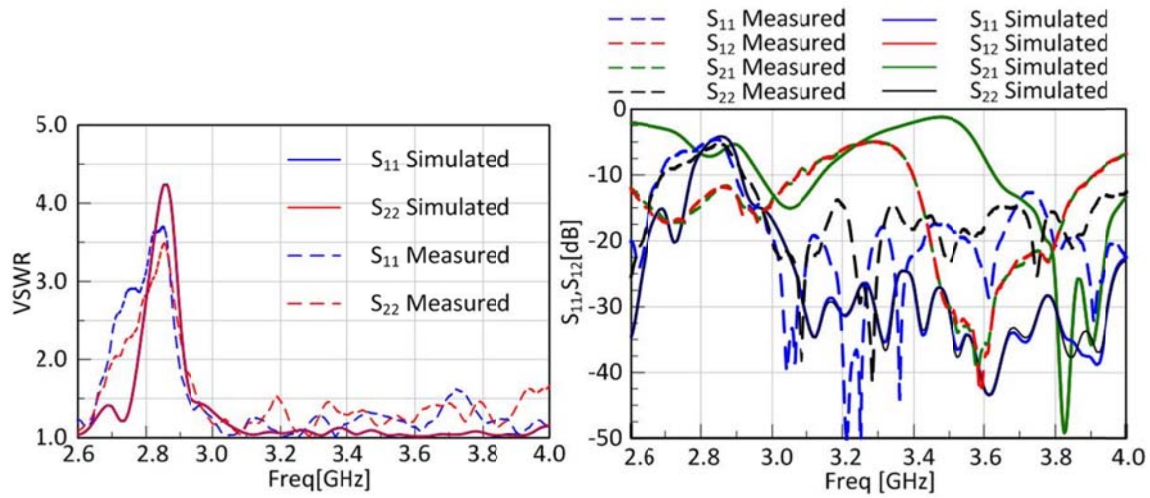

Fig. 66. Measured and simulated VSWR (left) and S-parameters (right).

The radiation patterns are shown in Fig. 67 for this configuration, where near-broadside radiation occurs at 3 GHz. As in the previous cases, measured results showed higher sidelobes due to faults in the placement of the cantilevers in the troughguide. Supporting the cantilevers with foam to create the tapering angles was not accurate enough to reproduce the desire distribution, but sufficient to approximate it.

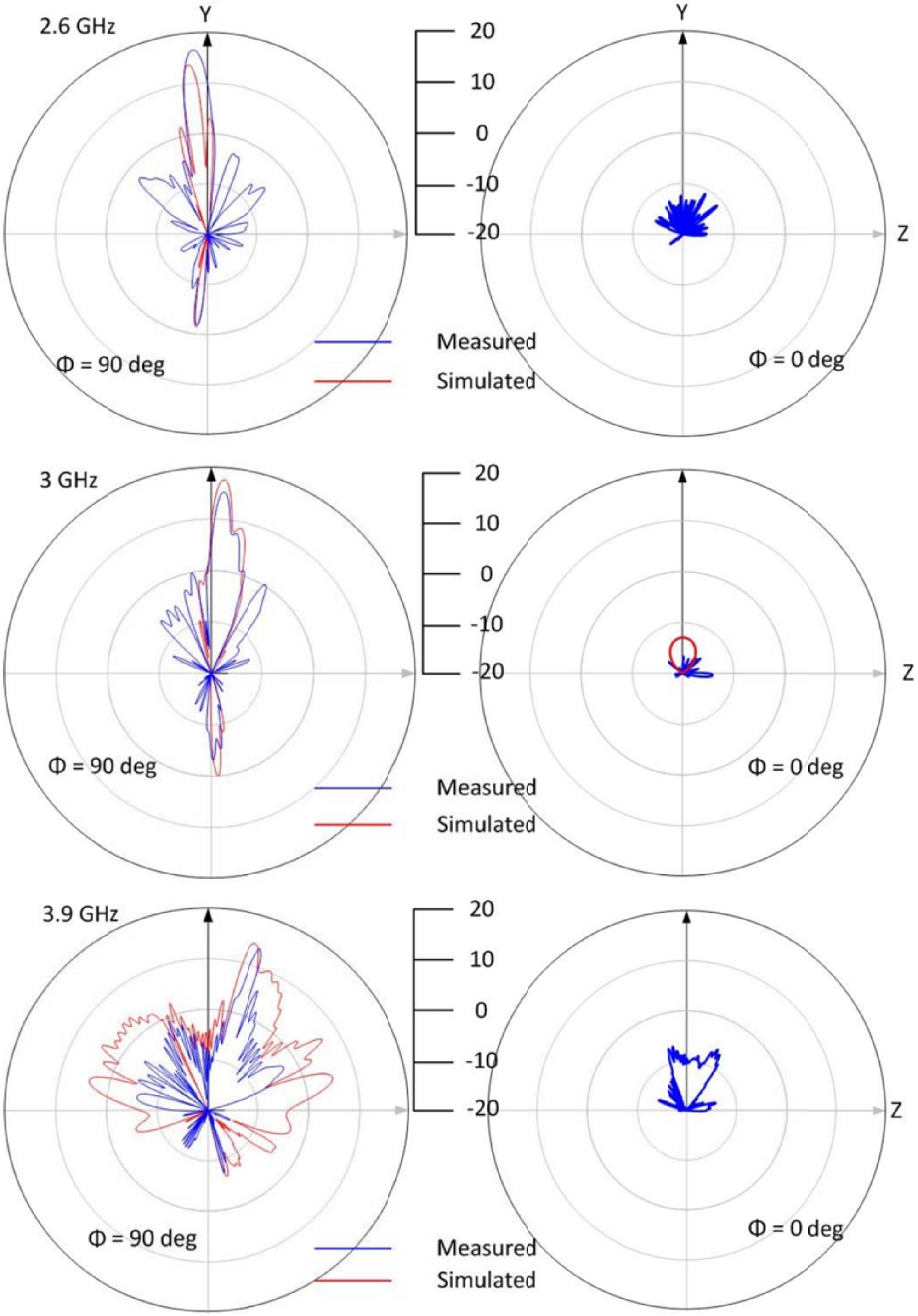

Fig. 67. Radiation patterns at the co-polarization and cross-polarization planes at 2.6 GHz, 3 GHz and 3.9 GHz.

4. *λ/2 Cantilevers with Two Holes*

Two quarter-wavelength long cantilevers (with two 8 mm radius holes) were examined next (Fig. 68) to verify that holes placed along the edge of half-wavelength long cantilever can reduce the reflections due to phase accumulation. Simulated and measured results in Fig. 69 (left) demonstrate this through the reduction in VSWR, and verify that the reflections due to the phase accumulation can be mitigated through this method and still achieve broadside radiation (Fig. 70).

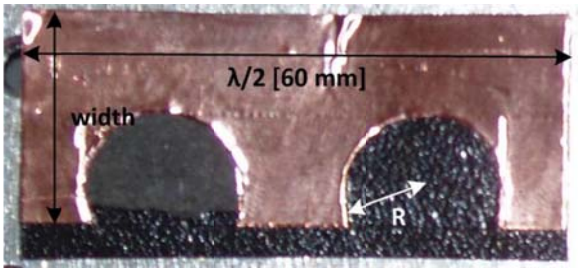

Fig. 68. Half wave long cantilever with two holes.

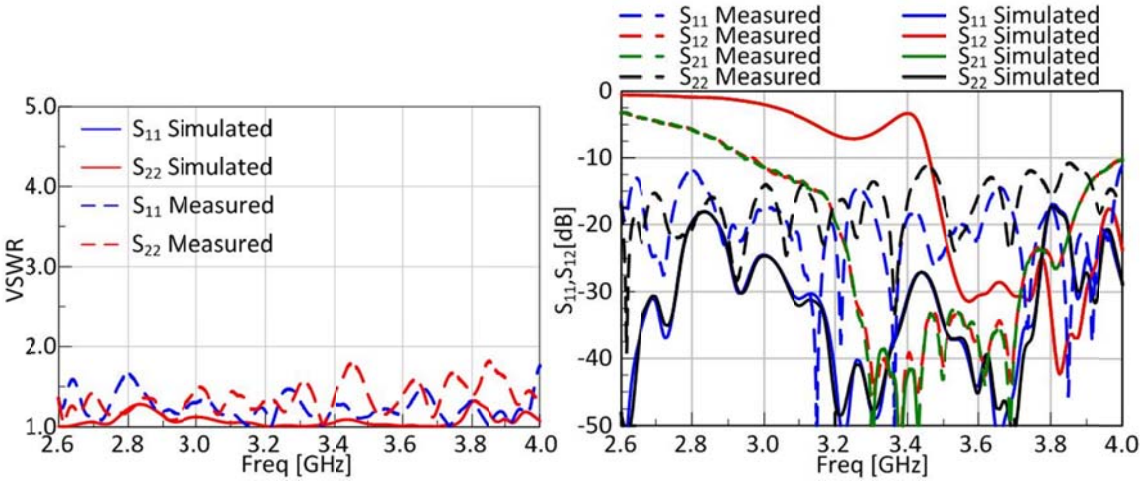

Fig. 69. Measured and simulated VSWR (left) and S-parameters (right).

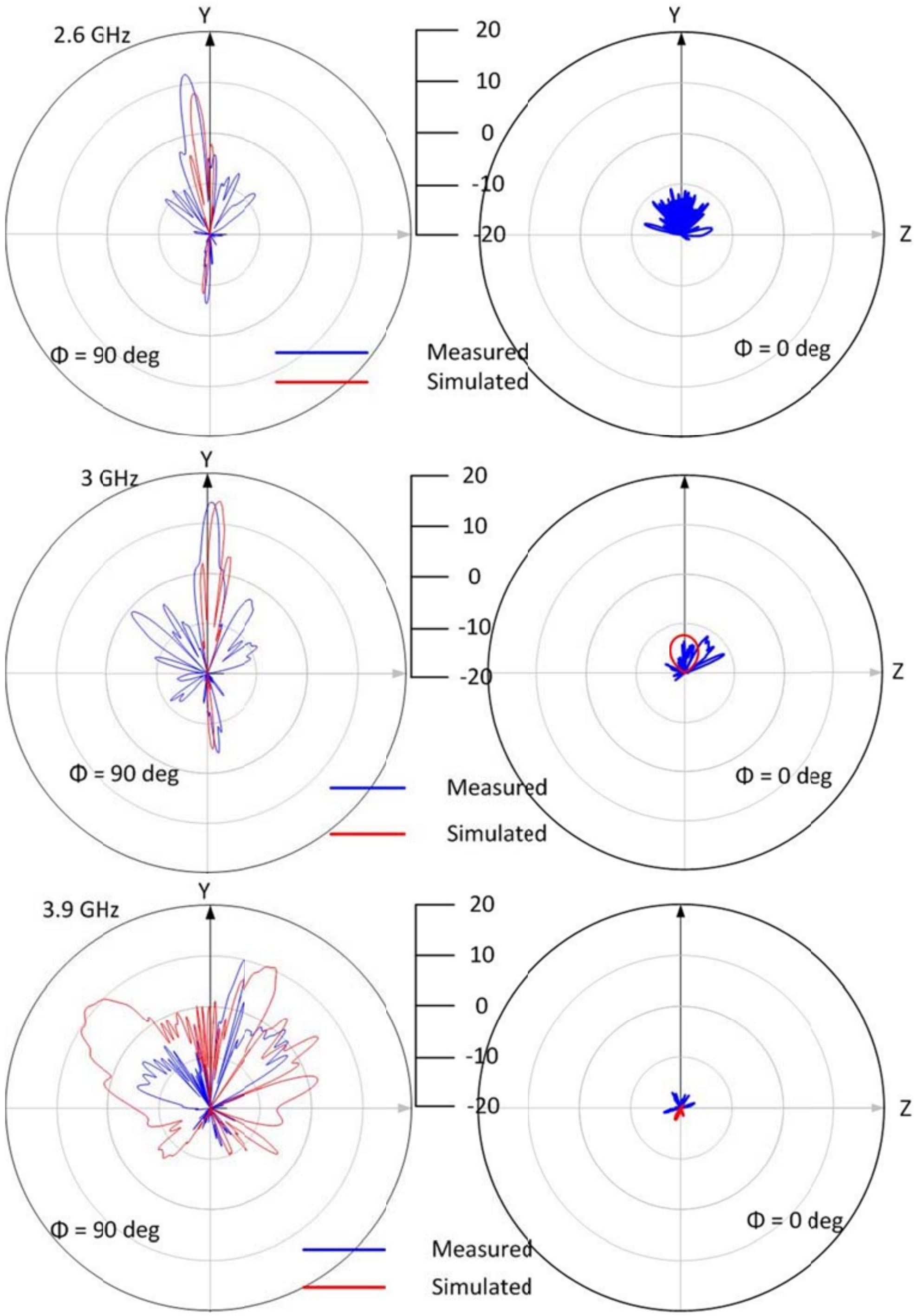

Fig. 70. Radiation patterns at the co-polarization and cross-polarization planes at 2.6 GHz, 3 GHz and 3.9 GHz.

5. 3λ/4 Cantilevers

Fig. 73 (lower right) shows three quarter-wavelength long cantilevers without holes that are actuated together at the same angle. The measured and simulated results for this scenario are shown in Fig. 71 with good agreement between the simulated and measured. A high peak is located at 3.6 GHz, where the system suffers from high reflections as it also seen from the S-parameter plots of Fig. 71(right). Radiation patterns at 2.6 GHz, 3 GHz and 3.9 GHz are shown in Fig. 72 for the co- and cross-polarizations. At 3 GHz the main beam points 20° away from broadside towards the forward quadrant.

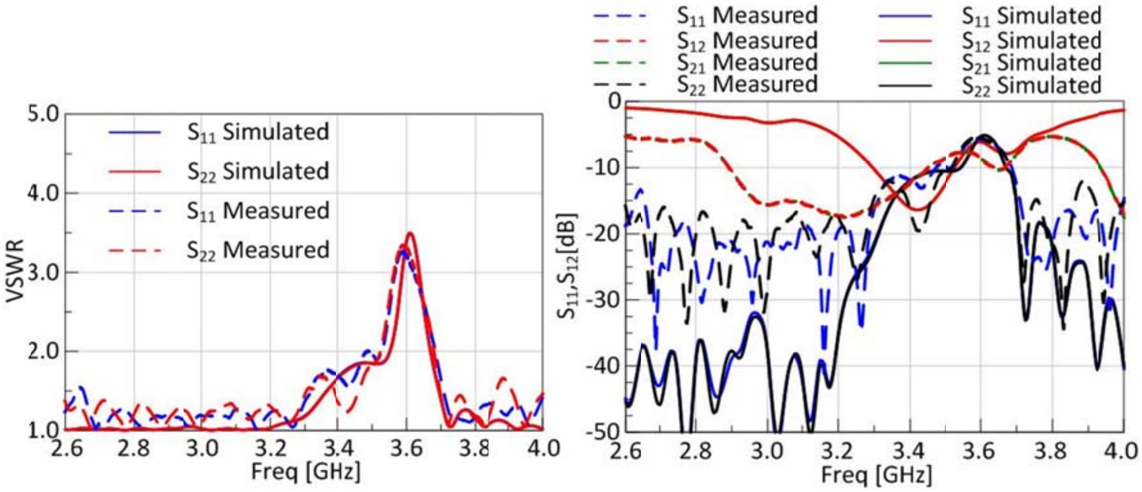

Fig. 71. Measured and simulated VSWR (left) and S-parameters (right).

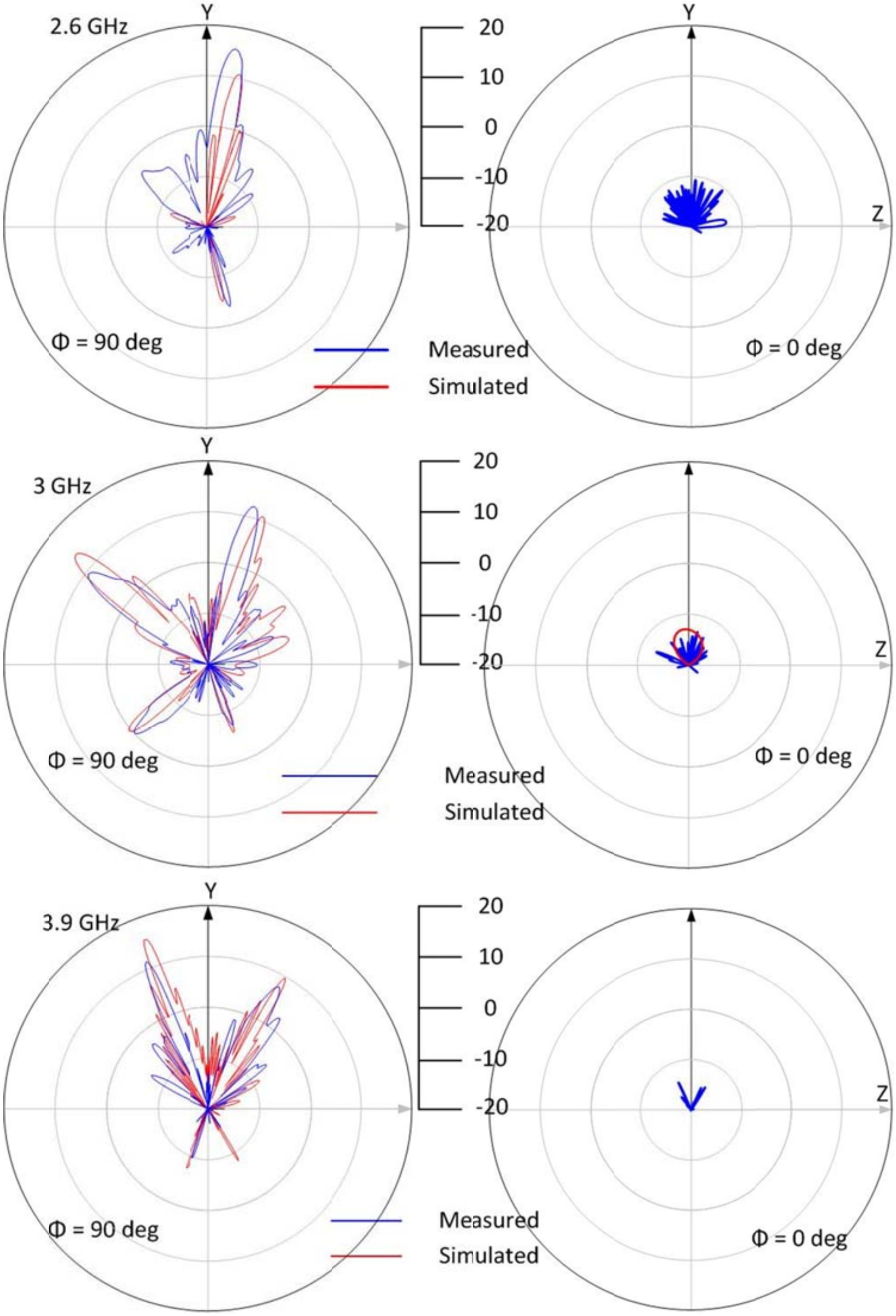

Fig. 72. Radiation patterns at the co-polarization and cross-polarization planes at 2.6 GHz, 3 GHz and 3.9 GHz.

6. 3λ/4 Cantilevers with Three Holes

Three quarter-wavelength long cantilevers (with three 8 mm radius holes were also examined (shown in Fig. 73, left). Simulated and measured results of the VSWR and S-parameters are shown in Fig. 74. A small peak can still be detected that is slightly shifted to the left as the cantilevers appear longer with the holes. Fig. 76 shows the radiation patterns where at 3 GHz, the main beam is located 20° from broadside towards the forward quadrant. Fig. 75 shows the network analyzer on an optics table and next to the TWA and S-Band waveguide calibration kit used for all the measurements in this thesis. The TWA is connected to the transition which is connected to a coax-to-waveguide adaptor and connected to the network analyzer through a coaxial cable.

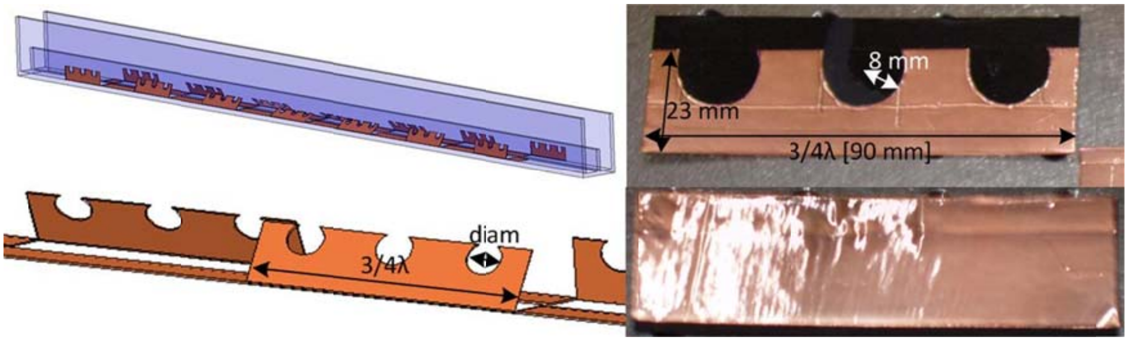

Fig. 73. Three quarter wave long cantilevers with and without holes in a TWG.

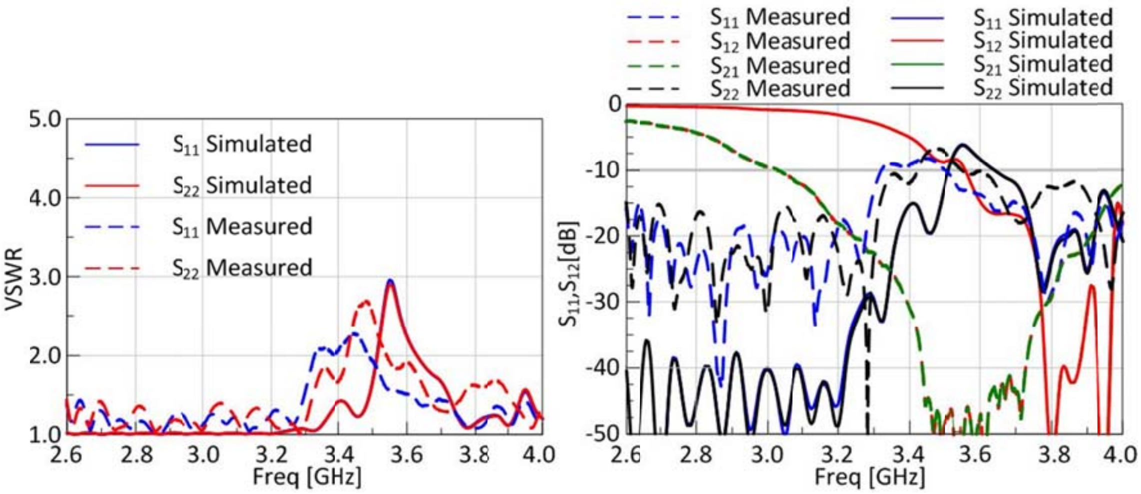

Fig. 74. Measured and simulated VSWR (left) and S-parameters (right).

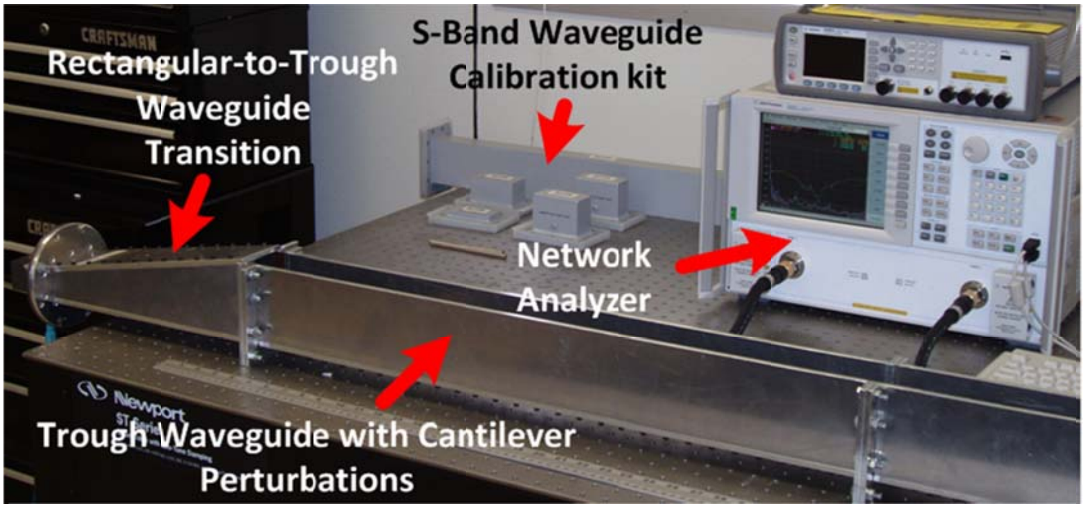

Fig. 75. The experimental setup used for measurements with the waveguide calibration kit, the network analyzer and the DUT.

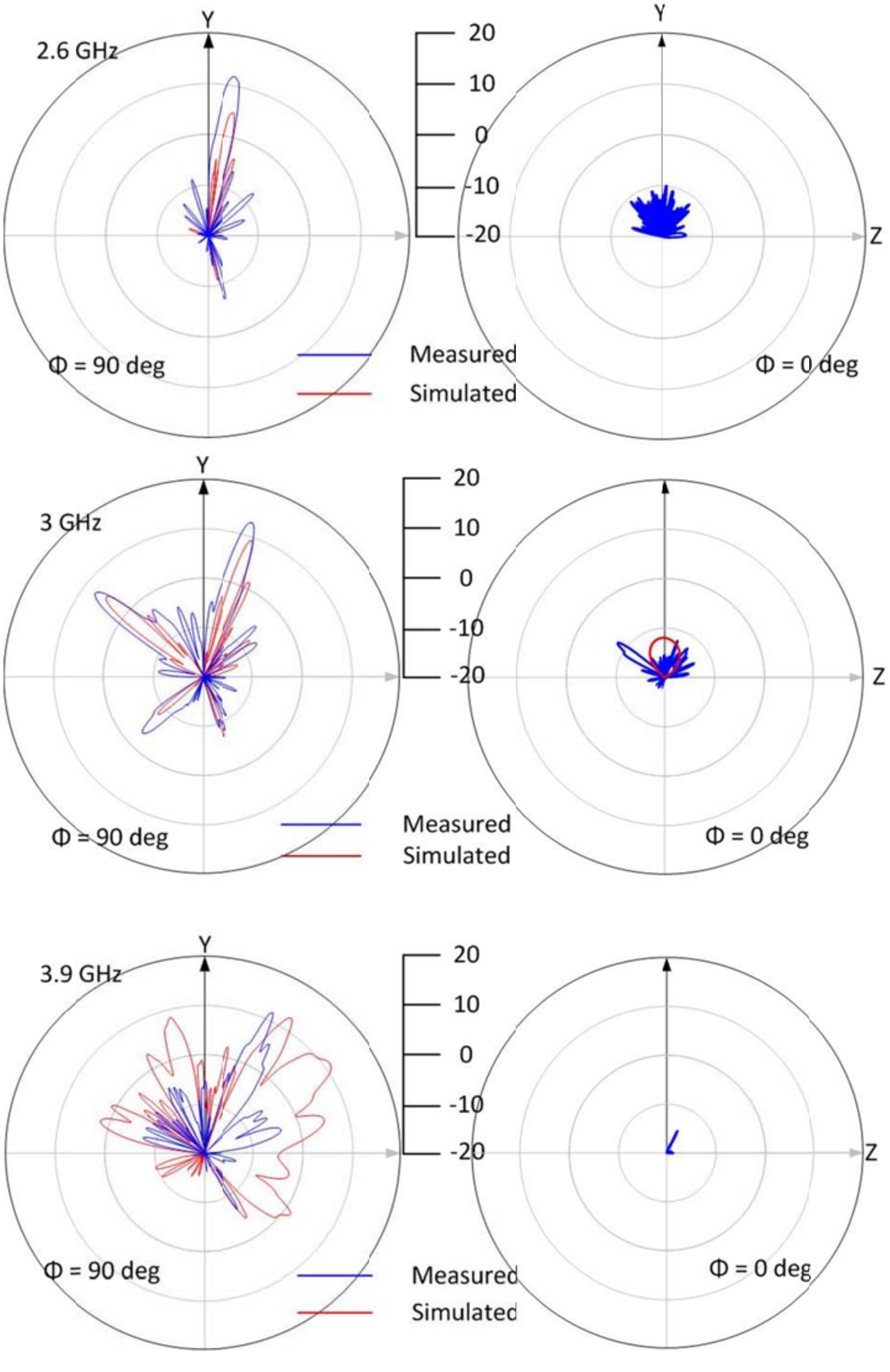

Fig. 76. Radiation patterns at the co-polarization and cross-polarization planes at 2.6 GHz, 3 GHz and 3.9 GHz.

Fig. 77 summarizes the reconfiguration of the radiation pattern by altering the cantilever length. The main beam can steer from the backward quadrant ($\lambda/4$) trough broadside ($\lambda/2$) towards the forward quadrant ($3\lambda/4$). The VSWR and attenuation of each beam direction, which demonstrates the concept that the main beam can be altered sufficiently by actuating different sets of cantilevers to create discretized lengths.

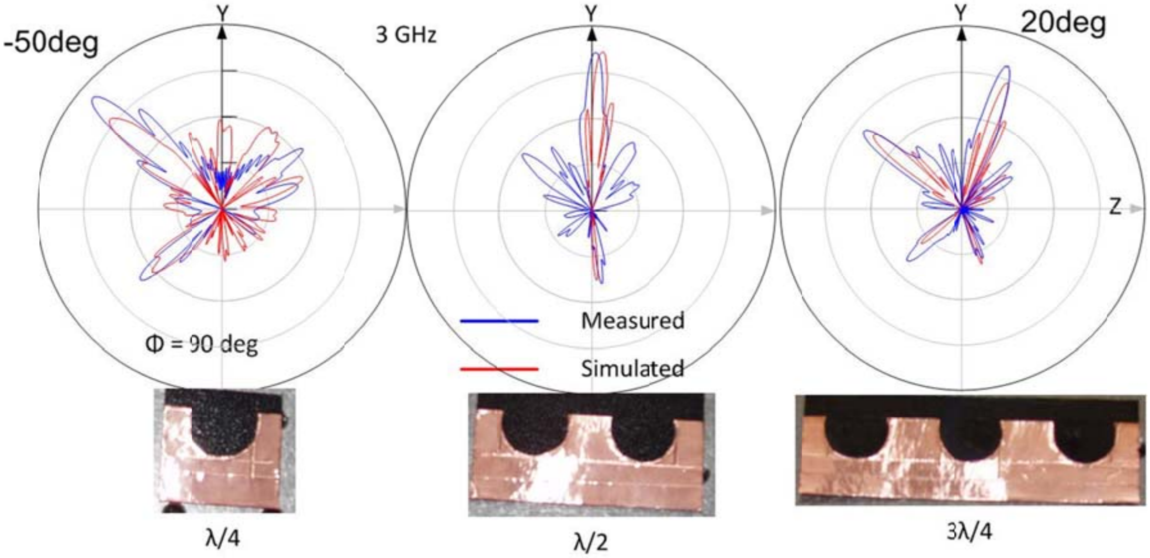

Fig. 77. Beam steering by changing the length of the cantilevers.

K. Aerodynamic Performance of the TWA with Cantilever Perturbations

The trough waveguide provides a rigid platform that integrates reconfigurable antennas and sensing mechanisms into the same device. The internal volume of these TWG structures can be exploited by sealing them with an electromagnetically transparent cover and using the topology for pressurized air-flow through the antenna. Finite elements simulations [18] were employed to study the aerodynamic performance and characteristics of the trough waveguide antenna with the cantilever perturbations as an extension of the aerodynamic performance of the RWG-to-TWG transition discussed in Ch.3. It was also shown that air flow through the transition is channelized between the sidewalls and the center fin. The presence of cantilevers in the TWA perturbs the airflow, creating vortices around the cantilevers where sensors and other devices can potentially be placed. Fig. 78 shows cut planes along the length inside the volume of the structure of the velocity and vorticity fields along with the vorticity streamlines.

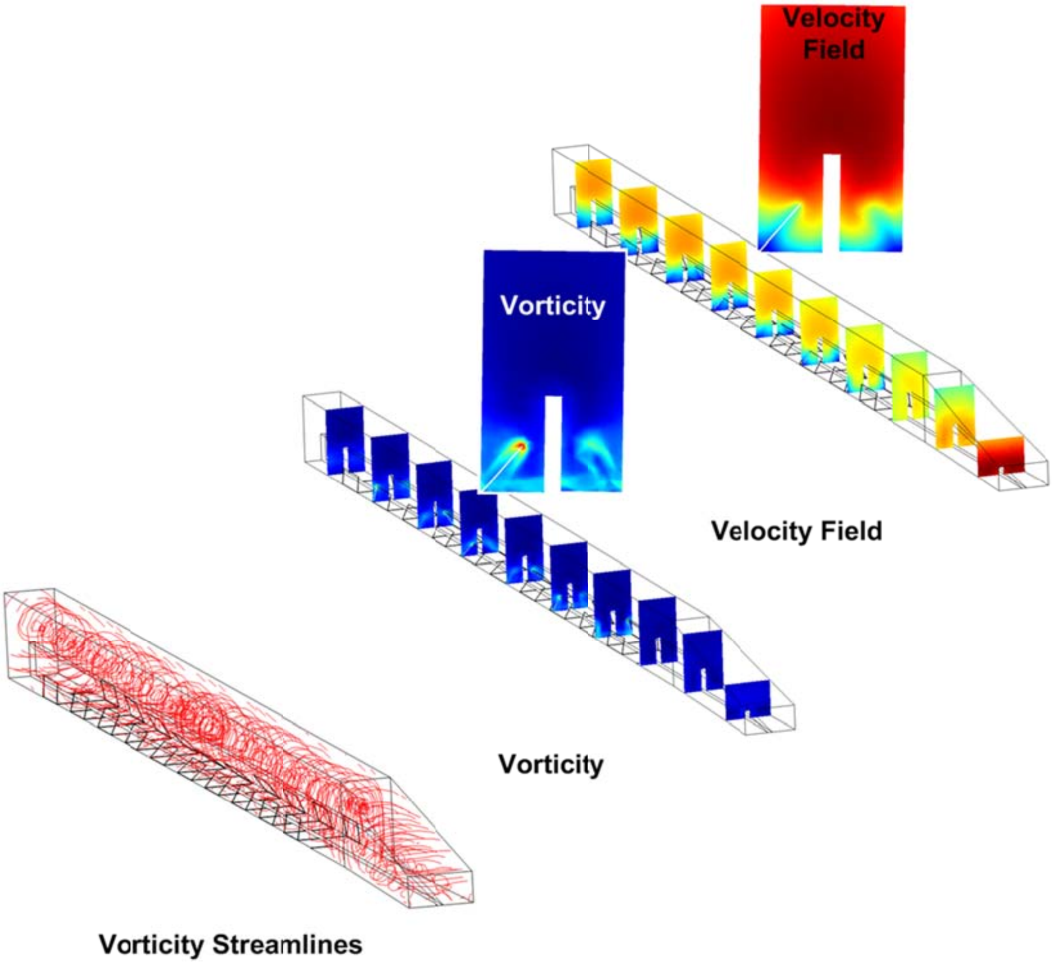

Fig. 78. Aerodynamic performance of the TWA with cantilevers.

CHAPTER V

FUTURE WORK

The foundations of developing a multifunctional device based on the troughguide antenna and waveguide platform with integrated sensing capabilities has been discussed in this thesis. Ongoing and future work will examine more TWA designs and evaluate "better" self-matching networks in the cantilever (spiral slots, etc.) to better mitigate phase accumulation. Further, a more extensive study of the aerodynamic performance will be undertaken to explore different setups and conditions under which the structure will perform (air tunnel tests, etc.). Finally, the development of sensor systems for certain applications is of interest to this work.

CHAPTER VI

CONCLUSIONS

The electromagnetic and aerodynamic co-design of a non-pyramidal RWG-to-TWG transition and fixed-frequency pattern reconfigurable TWA can provide many of the desirable characteristics required by a platform which integrates reconfigurable antennas and sensing mechanisms into the same device. An S-band design (2.6 GHZ to 3.95 GHz) of a non-pyramidal RWG-to-TWG transition was proposed for this. Simulated and measured results for a fabricated device validated this thesis by designing the structure to meet both its electromagnetic and aerodynamic performance requirements. The resulting pattern reconfigurable TWA using cantilever perturbations provided high gain and was also demonstrated using experimental and simulated results that showed scanning from the backward quadrant (-50°) to the forward quadrant (20°) can be achieved. Methods for treating high reflections due to phase accumulation problem at broadside were also discussed and as results showed how the requirements can be met.

REFERENCES

[1] F. Ishihara and S. Iiguchi, "Equivalent characteristic impedance formula of waveguide and its applications," *Electronics and Communications in Japan (Part II: Electronics),* vol. 75, pp. 54-66, 1992.

[2] J. L. Volakis, *Antenna Engineering Handbook,* 4th Edition, New York, McGraw Hill Professional, 2007.

[3] W. Rotman and A. A. Oliner, "Periodic structures in trough waveguide," *IRE Transactions on Microwave Theory and Techniques,* vol. 7, pp. 134-142, 1959.

[4] W. Rotman and N. Karas, "Some new microwave antenna designs based on the trough waveguide," in *IRE International Convention Record*, 1956, pp. 230-235.

[5] W. Rotman and A. Maestri, "An electromechanically scannable trough waveguide array," in *IRE International Convention Record*, 1960, pp. 67-83.

[6] W. Rotman and A. Oliner, "Asymmetrical trough waveguide antennas," *IRE Transactions on Antennas and Propagation,* vol. 7, pp. 153-162, 1959.

[7] G. H. Huff and A. S. Long, "Reconfigurable radiation from a W-band trough waveguide antenna: trade-offs in impedance and radiation from tapered MEMS-based perturbations," in *Proc. of the IEEE Antennas and Propagation Society International Symposium,* pp. 109-112, 2007.

[8] C. M. Rappaport and F. R. Morgenthaler, "Localized hyperthermia with electromagnetic arrays and the leaky-wave troughguide applicator," *IEEE Transactions on, Microwave Theory and Techniques,* vol. 34, pp. 636-643, 1986.

[9] G. Sauve, M. Moisan, Z. Zakrzewski and C. A. Bishop, "Sustaining long linear uniform plasmas with microwaves using a leaky-wave (troughguide) field applicator," *IEEE Transactions on Antennas and Propagation,* vol. 43, pp. 248-256, 1995.

[10] G. D. Hopkins, B. K. Edenfield, J. G. Hampton and R. L. Roberts, "A new coax to troughguide transition," *IEEE Microwave and Wireless Components Letters,* vol. 12, pp. 299-301, 2002.

[11] HFSS V12.0: Ansoft corperation, Pittsburgh, PA 15219, http://www.ansoft.com/products/hf/hfss/ .

[12] N. C. Albertsen and P. Skov-Madsen, "A compact septum polarizer," *IEEE Transactions on Microwave Theory and Techniques,* vol. 31, 1983, pp. 654-660.

[13] J. Bornemann and V. A. Labay, "Ridge waveguide polarizer with finite and stepped-thickness septum," *IEEE Transactions on* n *Microwave Theory and Techniques,* vol. 43, pp. 1782-1787,1995.

[14] V. K. Lakshmeesha,G. S. Seetharaman, U. Prabhakaran,V. V. Srinivasan, L. Nicholas, *et al.*, "A compact high power S-band dual frequency, dual polarised feed," in *Proc. of the IEEE Antennas and Propagation Society International Symposium,* vol.3, pp. 1607-1610, 1991.

[15] J. H. Hinken,K. Jedamski and F. Henze, "Design of sloping septum polarizers using coupled wave equations," in*, Proc. 16th European Microwave Conference*, pp. 423-428, 1986.

[16] S. Hopfer, "The design of ridged waveguides," *IRE Transactions on Microwave Theory and Techniques,* vol. 3, pp. 20-29, 1955.

[17] S. B. Cohn, "Properties of ridge wave guide," in *Proc. of the IRE,* vol. 35, pp. 783-788, 1947.

[18] Comsol V3.5: Comsol, Inc., Stockholm, Sweden, http://www.comsol.com/.

[19] R. Collin, *Foundations for Microwave Engineering,* New York, Wiley-IEEE Press, 2001.

[20] R. Collin, *Field Theory of Guided Waves*: New York, Wiley-IEEE Press, 1990.

[21] R. E. Collin, "The optimum tapered transmission line matching section," in *Proc. of the IRE,* vol. 44, pp. 539-548, 1956.

[22] H. C. Early, "A wide-band directional coupler for wave guide," in *Proc. of the IRE,* vol. 34, pp. 883-886, 1946.

[23] R. Elliott, *Antenna Theory & Design*: New York, Wiley-IEEE Press, 2003.

[24] R. Harrington, *Time-Harmonic Electromagnetic Fields*: New York, Wiley-IEEE Press 2001.

[25] D. M. Pozar, *Microwave Engineerin*g, 3th ed., New York, John Wiley & Sons, Inc, 2005.

[26] L. Loizou, F. J. Drummond, G. H. Huff, "Electromagnetic and aerodynamic performance of a rectangular-to-trough waveguide transition and troughguide antenna with cantilever perturbations and high Reynolds number air flow," in *Proc. 2010 IEEE/URSI Int. Symp. Antennas and Propagation*, Toronto, Canada, July, *ses.308.8, 2010.*

APPENDIX A

A. Matlab script for deembedding using ABCD-parameters

```
%----------------Deembedding the transitions-----------------
%
%----------------Loizos Loizou-------------------------------
%----------------Texas A&M University------------------------
%----------------October 2010-------------------------------
%
%Convert the measured data from db to watts and into a complex form.
%First column of the data is the frequency, second is the S11 in db and
the %third is the phase of S11.Same applies for all S parameters.

data = data;
S_11=10.^((data(:,2))./10);
S_21=10.^((data(:,4))./10);
S_12=10.^((data(:,6))./10);
S_22=10.^((data(:,8))./10);
F=data(:,1).*1e-9;
%In order to perform calculations using the build in functions s2abcd
is
%needed that the data are arranged into a 2x2xm matrix.
n=20501;
for i=1:n
sparam(1,1,i)=S_11(i,1);
sparam(1,2,i)=S_12(i,1);
sparam(2,1,i)=S_21(i,1);
sparam(2,2,i)=S_22(i,1);
end;
abcd_params = s2abcd(sparam,50); %s to abcd parameters

%for solving the system for A,B,C,D parameters
syms a b c d am bm cm dm

[a b c d] = solve(a.^2+b.*c-am,a.*b+b.*d-bm,a.*c+c.*d-cm,b.*c+d.^2-
dm,'a','b','c','d');
am = abcd_params(1,1,:);
bm = abcd_params(1,2,:);
cm = abcd_params(2,1,:);
dm = abcd_params(2,2,:);
a_m(1,:)=am;
am=a_m;
b_m(1,:)=bm;
bm=b_m;
c_m(1,:)=cm;
cm=c_m;
```

```
d_m(1,:)=dm;
dm=d_m;
a = eval(vectorize(a(1)));
b = eval(vectorize(b(1)));
c = eval(vectorize(c(1)));
d = eval(vectorize(d(1)));
%creat again a 2x2xm matrix with all the ABCD parameters and convert
back
%to S parameters.
for i=1:n
abcd(1,1,i)=a(1,i);
abcd(1,2,i)=b(1,i);
abcd(2,1,i)=c(1,i);
abcd(2,2,i)=d(1,i);
end;
s_params = abcd2s(abcd,50);

for i=1:n
    Single_connector_S_P(:,1)=F;
    Single_connector_S_P(i,2)=10.*log10(abs(s_params(1,1,i)));
    %Single_connector_S_P(i,3)=angle(s_params(1,1,i));
    Single_connector_S_P(i,3)=10.*log10(abs(s_params(1,2,i)));
    %Single_connector_S_P(i,5)=angle(s_params(1,2,i));
    Single_connector_S_P(i,4)=10.*log10(abs(s_params(2,1,i)));
    %Single_connector_S_P(i,7)=angle(s_params(2,1,i));
    Single_connector_S_P(i,5)=10.*log10(abs(s_params(2,2,i)));
    %Single_connector_S_P(i,9)=angle(s_params(2,2,i));
end;
figure
    plot(F,Single_connector_S_P(:,3));
    title('S12');
```

B. Matlab script of the transition impedance model

```
% Impedance Model of the Taper Transition ----  Rectangular WG model
%
%------------------Loizos Loizou--------------------------------
%------------------Texas A&M University-------------------------
%------------------October 2010--------------------------------
%
%----------------------------------------------------------------
%This script reads the waveguide dimensions from an excel file,
%calculates the cutoff frequency and the real part of the
%characteristic impedance of the waveguide at 3GHz for both troughguide
%and rectangular sides.

close all;
clear all;
clc;
data = xlsread('TransitionData_Chen2.xls');
no=120*pi;
eo=8.854e-12;
mo=pi*4e-7;
c=3e8;
h=data(:,4)./1000;
a2=data(:,2)./1000;
t=data(:,3)./1000;
ext=data(:,8)./1000;
b1=data(:,5);
b2=data(:,6);
a1=data(:,7)/1000;
L=320;
%f=2.5e9:0.46e8:4e9;
f=3e9;
%lamda=1000*c./f;
x=0:10:L;
x2=sort(x','descend');
fc1=1./(2.*a1'.*(eo*mo)^0.5);
fc2 = 1./(2.*(2.*h+2.*ext+2*t).*(eo*mo)^0.5);
Zo1=(no)./(sqrt(1-((fc1./f).^2)));
Zo2=(no)./(sqrt(1-((fc2./f).^2)));
Rrect= 0.58*(real(Zo1'));
Rtrough = 0.255*real(Zo2);

figure (1);
plot(x2,Rrect,'red');
title('Resistance');
hold on
plot(x2,Rtrough);
```

VITA

Name: Loizos Loizou

Address: 214 Zachry Engineering Center, TAMU 3128, College Station,
Texas 77843-3128

Email Address: lloizos@gmail.com
loizos@neo.tamu.edu

Education: M.S., Electrical Engineering, Texas A&M University, 2010

Diploma in Electrical and Computer Engineering, National Technical University of Athens, 2008